

Naval Research Laboratory

Washington, DC 20375-5320

AD-A270 734



NRL/MR/7234--93-7401

Modeling of Current Features in Gulf Stream SAR Imagery

R. W. JANSEN
S. R. CHUBB
R. A. FUSINA
G. R. VALENZUELA

*Imaging Systems and Research Branch
Remote Sensing Division*

September 13, 1993

DTIC
ELECTE
OCT 15 1993

D

Approved for public release; distribution unlimited.

93-24124



REPORT DOCUMENTATION PAGE			Form Approved OMB No. 0704-0188	
Public reporting burden for this collection of information is estimated to average 1 hour per response, including the time for reviewing instructions, searching existing data sources, gathering and maintaining the data needed, and completing and reviewing the collection of information. Send comments regarding this burden estimate or any other aspect of this collection of information, including suggestions for reducing this burden, to Washington Headquarters Services, Directorate for Information Operations and Reports, 1216 Jefferson Davis Highway, Suite 1204, Arlington, VA 22202-4302, and to the Office of Management and Budget, Paperwork Reduction Project (0704-0188), Washington, DC 20503.				
1. AGENCY USE ONLY (Leave Blank)	2. REPORT DATE September 13, 1993	3. REPORT TYPE AND DATES COVERED Interim Report on Continuing NRL Problem		
4. TITLE AND SUBTITLE Modeling of Current Features in Gulf Stream SAR Imagery			5. FUNDING NUMBERS 61153N-21 RR021-05-4G	
6. AUTHOR(S) Robert W. Jansen, Scott R. Chubb, Robert A. Fusina, and Gasper R. Valenzuela				
7. PERFORMING ORGANIZATION NAME(S) AND ADDRESS(ES) Naval Research Laboratory Washington, DC 20375-5320			8. PERFORMING ORGANIZATION REPORT NUMBER NRL/MR/7234-93-7401	
9. SPONSORING/MONITORING AGENCY NAME(S) AND ADDRESS(ES) Department of the Navy Office of Naval Research Arlington, VA 22217-5660			10. SPONSORING/MONITORING AGENCY REPORT NUMBER	
11. SUPPLEMENTARY NOTES				
12a. DISTRIBUTION/AVAILABILITY STATEMENT Approved for public release; distribution unlimited.			12b. DISTRIBUTION CODE	
13. ABSTRACT (Maximum 200 words) The theoretical formulation, numerical implementation, and testing of NRL's recently developed time-dependent ocean wave model (NTOW) is described. The propagation of the wave field is computed via the action density conservation equation for general time varying currents, winds, and bathymetry. The NTOW model is used to predict wave-current interaction effects in a region of strong surface convergence near the edge of the Gulf Stream off Cape Hatteras. The computed wave field is used in conjunction with a composite scattering radar model to derive radar imagery. Our radar predictions are compared with real aperture radar data collected during the NRL high-resolution remote sensing experiment (Valenzuela, 1991).				
14. SUBJECT TERMS Remote sensing Ocean currents Wave-current interaction Gulf Stream SAR imagery			15. NUMBER OF PAGES 57	
			16. PRICE CODE	
17. SECURITY CLASSIFICATION OF REPORT UNCLASSIFIED	18. SECURITY CLASSIFICATION OF THIS PAGE UNCLASSIFIED	19. SECURITY CLASSIFICATION OF ABSTRACT UNCLASSIFIED	20. LIMITATION OF ABSTRACT UL	

CONTENTS

1. Introduction	1
2. Wave-Action Formalism	2
3. Model	6
4. Testing	11
5. Rip Feature	14
6. Summary	19
Acknowledgements	21
References	22
Appendix A: Equilibrium Spectrum	25
Appendix B: Convergence of Wave Models with Grid Spacing	29

DTIC QUALITY INSPECTED 2

Accession For	
NTIS CRA&I	<input checked="checked" type="checkbox"/>
DTIC TAB	<input type="checkbox"/>
Unannounced	<input type="checkbox"/>
Justification	
By	
Distribution	
Availability Codes	
Dist	Avail and/or Special
A-1	

MODELING OF CURRENT FEATURES IN GULF STREAM SAR IMAGERY

1. Introduction

Interpretation of ocean radar imagery from regions involving strong current flows, such as the Gulf Stream, is possible only if the link between observed radar features and the underlying depth and surface current structure is sufficiently understood. Because the radar effectively maps the surface waves, this link requires knowledge of the effects of wave-current/depth interactions on the wind-wave field. These effects must be understood for a wide range of wavelengths; waves on the 1 m or larger scales lead to tilt modulation effects in the radar image and cm-scale waves affect the radar return as Bragg scatterers. These modulations in the wave field often lead to sharp features in radar imagery even for relatively mild current/depth variations. These features are produced by both advective and refractive effects which can alter the size and propagation direction of the waves. An obvious example of refractive effects on waves is evident in coastal regions where a sloping beach tends to orient the propagation direction of waves toward the shore. Waves in coastal areas are also significantly affected by current-depth variations in tidal inlets or near the mouths of rivers. The refractive effect of the gulf stream current on the propagation of long transatlantic ocean waves is also easily observed and well understood. Much less is known about the wave-current interaction for shorter waves (1 cm to 100 m), which often is a dominant factor in the formation of high intensity variations in the radar return that are frequently observed in real and synthetic aperture radar imagery.

To investigate current depth features in the ocean, NRL has developed a Time-dependent Ocean Wave (NTOW) model which allows for general time varying depth, current, and wind fields. The model uses conservation of wave action to compute the propagation of a statistical wind wave field. The action density formalism is presented in section 2, and the NTOW model implementation of the solution of the action density conservation equation using a finite step scheme is described in section 3. Tests of the NTOW model are presented in section 4. In section 5 we present NTOW predictions for the wind wave field and radar return for a current model of the "Rip" feature which appeared in NRL high resolution Real Aperture Radar (RAR) imagery of a boundary region of the Gulf Stream off Cape Hatteras. Section 6 summarizes.

2. Wave-Action Formalism

2.1. Dispersion Relation

For surface gravity-capillary waves in the linear approximation in the absence of currents the dispersion relation relating the wavenumber k and the intrinsic frequency ω_o is

$$\omega_o^2 = gk \tanh kd \left[1 + \frac{T}{\rho g} k^2 \right], \quad (1)$$

where g is the acceleration of gravity, d is the water depth, T is the surface tension, and ρ is the water density. The wave crests propagate at the phase speed c given by the ratio,

$$c = \frac{\omega_o}{k}, \quad (2)$$

whereas the wave energy propagates at the group speed c_g given by

$$c_g = \frac{\partial \omega_o}{\partial k} = \left[\frac{1}{2} + \frac{kd}{\sinh 2kd} + \frac{1}{1 + \frac{\rho g}{Tk^2}} \right] \frac{\omega_o}{k}. \quad (3)$$

When non-zero currents are present the frequency of the waves observed in the rest frame will be Doppler shifted. The frequency in the rest frame ω is related to the local intrinsic frequency ω_o (in the moving frame) by,

$$\omega = \omega_o + \mathbf{k} \cdot \mathbf{U}. \quad (4)$$

It is interesting to observe that for sufficiently large currents the second term in Eq. 4 can become comparable to ω_o . In this case, the frequency of the waves opposing the current and their energy propagation speed, $c_g + \hat{\mathbf{k}} \cdot \mathbf{U}$, can vanish leading to the phenomenon of wave blocking.

2.2. Wave Action Density Equation

For slowly varying mean fields the evolution of the wave spectrum is most easily modeled in terms of the wave action density formalism [cf. G.B. Whitham, 1967; F.P. Bretherton and C.J.R. Garrett, 1968]. The wave field is regarded as a superposition of waves, such that the free surface displacement $\xi(x,t)$ can be represented by a Fourier-Stieltjes sum,

$$\xi(x,t) = \sum_k \left\{ \eta_k e^{i(k \cdot x - \omega t)} + \eta_k^* e^{-i(k \cdot x - \omega t)} \right\}, \quad (5)$$

where η_k is a random Fourier amplitude. For a homogeneous, stationary wave field η_k satisfies

$$\langle \eta_k \eta_{k'}^* \rangle = E(k) \frac{k \Delta k}{2\rho\omega_o^2} \delta_{kk'} = F(k) \frac{\Delta k}{2} \delta_{kk'}, \quad (6)$$

where Δk is the two dimensional wavenumber increment, $E(k)$ is the energy density spectrum, and $F(k)$ is the variance density spectrum satisfying

$$\int \int F(k) dk = \langle \xi^2 \rangle. \quad (7)$$

In the absence of depth or current variations the variance spectrum is conserved along ray paths. However, when current or depth variations are present F is no longer conserved due to the variations in the frequency along these ray paths. The wave action density defined by

$$N(k;x,t) = \frac{E(k;x,t)}{\omega_o} = \frac{\rho\omega_o}{k} F(k;x,t) \quad (8)$$

however, remains constant along ray paths even for variable depths and currents when no energy sources or sinks are present. The wave action density conservation equation for a source S can be written as

$$\frac{DN}{Dt} = \frac{\partial N}{\partial t} + \dot{x} \cdot \nabla_x N + \dot{k} \cdot \nabla_k N = S \quad (9)$$

where the time derivatives \dot{x} and \dot{k} are related to the frequency ω through the characteristic equations

$$\dot{x} = \nabla_k \omega, \quad \dot{k} = -\nabla_x \omega. \quad (10a,b)$$

Using Cartesian spacial coordinates (x,y) , and polar wavevector coordinates (k,θ) :

$$k = \sqrt{k_x^2 + k_y^2}, \quad \theta = \tan^{-1} \left[\frac{k_y}{k_x} \right], \quad (11a,b)$$

the action density equation (Eq. 9) becomes

$$\frac{\partial N}{\partial t} + c_x \frac{\partial N}{\partial x} + c_y \frac{\partial N}{\partial y} + c_k \frac{\partial N}{\partial k} + c_\theta \frac{\partial N}{\partial \theta} = S, \quad (12)$$

where, for current field $U = (u,v)$, the coefficients c_i are

$$c_x = c_g \cos \theta + u \quad (13)$$

$$c_y = c_g \sin \theta + v, \quad (14)$$

$$c_k = \frac{-k\omega_o}{\sinh(2kd)} \left[\frac{\partial d}{\partial x} \cos \theta + \frac{\partial d}{\partial y} \sin \theta \right] - k \left[\frac{\partial u}{\partial x} \cos^2 \theta + \left(\frac{\partial v}{\partial x} + \frac{\partial u}{\partial y} \right) \cos \theta \sin \theta + \frac{\partial v}{\partial y} \sin^2 \theta \right], \quad (15)$$

$$c_\theta = \frac{-\omega_o}{\sinh(2kd)} \left[\frac{\partial d}{\partial x} \sin \theta - \frac{\partial d}{\partial y} \cos \theta \right] - \left[\frac{\partial u}{\partial y} \cos^2 \theta + \left(\frac{\partial v}{\partial y} - \frac{\partial u}{\partial x} \right) \cos \theta \sin \theta - \frac{\partial v}{\partial x} \sin^2 \theta \right] \quad (16)$$

where we have used Eqs. 1, 3, 4, and 10 to write the time derivatives of x and k in terms of the group velocity and gradients of the depth and currents.

2.3. Source Term

The source term S includes input from the wind, nonlinear wave-wave interactions, dissipation from such processes as wave breaking and bottom friction, surfactant damping, and other processes which generate or dissipate energy. Although the different processes are inherently interconnected, following Hasselmann [1968], the source is often written as a sum of separate terms (weak interaction approximation):

$$S = S_{in} + S_{nl} + S_{ds} \quad (17)$$

where S_{in} represents input from the wind, S_{nl} describes the nonlinear wave-wave interactions, and S_{ds} includes all dissipation terms. Many of the source terms are poorly understood and a number of competing expressions have been developed to describe them. The terms S_{in} and S_{ds} are usually expressed as relatively simple analytic functions which are linear in N . The nonlinear term S_{nl} is far more complicated involving integration over resonant k -vectors in a five dimensional phase space. Perturbative expressions for the nonlinear interaction have been derived for both gravity waves [Hasselmann, 1962], and capillary waves [Valenzuela, 1972; van Gastel, 1987]. However, computing these integrals directly is exceedingly costly and becomes impractical for most realistic situations. It is likely that little progress in wind wave modeling will be made with these first-principles approaches unless significant simplifications to the nonlinear source terms can be found. Presently, a few such simplifications have been developed and incorporation of these schemes into our model is in progress.

A far more simple form for the source term which is often sufficiently accurate for the description of short waves in mild current gradients was suggested by Hughes [Hughes, 1978].

In this approach the source is expressed as a Taylor series expansion in powers of N . To second order we have

$$S = \alpha + \beta N + \gamma N^2. \quad (18)$$

The constant term α has been associated with input from the wind through the Phillips turbulent resonant mechanism (Phillips, 1957), but is not included in our model. Rather, we assume that the source disappears for zero action density. The linear term βN is then the dominant term for small N and can be interpreted as the initial growth term S_{in} due to input from the wind. The initial growth of waves by wind has been investigated in detail by theory and experiments (for example see Plant, [1982]). Finally, the coefficient γ can be set by the requirement that the total source S should vanish as N approaches its equilibrium value N_o . This condition fixes γ to $-\beta/N_o$. The Hughes source can then be written:

$$S = -\beta N \frac{(N - N_o)}{N_o}. \quad (19)$$

Physically this source tries to mimic a true source by pushing the system toward a known equilibrium in regions of uniform current. This form of the source has been fully implemented into our model. However, it is applicable only for small current gradients and must be used with caution since it has no firm foundation in first principles.

3. Model

To solve the action density equation we use a finite differencing scheme which updates the action density at each time step. The action density equation (12) must be solved for a specified grid of x , y , k , θ , and t . Finite step methods often lead to instabilities for such multidimensional systems if sufficient care is not exercised in the numerical procedure. Our method closely follows the scheme implemented in WAVEWATCH described by Tolman [1991]. However, we use the (k, θ) space formalism rather than the (ω, θ) space method implemented in WAVEWATCH. In this scheme the propagation terms and source terms are

handled in separate time steps. The propagation is done using a predictor-corrector Crank-Nickolson procedure. The corrector is central in both space and time and the predictor is forward in time and central in space. To illustrate the method consider the simplified propagation equation (x-space only):

$$\frac{\partial N(x,t)}{\partial t} + c_x \frac{\partial N(x,t)}{\partial x} = 0. \quad (20)$$

The action is updated one time step as follows:

Predictor:

$$N_p(x_i, t_{n+1}) = N(x_i, t_n) - \frac{\Delta t c_x}{2 \Delta x} [N(x_{i+1}, t_n) - N(x_{i-1}, t_n)]. \quad (21)$$

Half-Time Value:

$$N_h(x_i, t_{n+1/2}) = \frac{1}{2} [N(x_i, t_n) + N_p(x_i, t_{n+1})]. \quad (22)$$

Corrector:

$$N(x_i, t_{n+1}) = N(x_i, t_n) - \frac{\Delta t c_x}{2 \Delta x} [N_h(x_{i+1}, t_{n+1/2}) - N_h(x_{i-1}, t_{n+1/2})]. \quad (23)$$

If this procedure is used without modification spurious solutions or negative action can occur. As discussed in Tolman these are avoided by adding a diffusion term in the spacial dimensions, using a limited flux approach in k -space, and using a conservative elimination scheme in θ -space. Adopting the more compact notation $N(i,j,k,l,n) = N(x_i, y_j, k_k, \theta_l, t_n)$, the complete five-dimensional action density equation for the predictor (the corrector has the same structure) then has the form:

$$N_p(i,j,k,l,n+1) = N(i,j,k,l,n) + \Delta t [L_x + L_y + L_k + L_\theta] \quad (24)$$

where

$$L_x = \frac{c_x}{2\Delta x} [(1-\alpha) N(i+1,j,k,l,n) + 2\alpha N(i,j,k,l,n) - (1+\alpha) N(i-1,j,k,l,n)] \quad (25)$$

$$L_y = \frac{c_y}{2\Delta y} [(1-\alpha) N(i,j+1,k,l,n) + 2\alpha N(i,j,k,l,n) - (1+\alpha) N(i,j-1,k,l,n)] \quad (26)$$

$$L_k = \frac{1}{k \Delta(\ln k)} [M(i,j,k+1/2,l,n) - M(i,j,k-1/2,l,n)] \quad (27)$$

$$L_\theta = \frac{c_\theta}{2\Delta\theta} [N(i,j,k,l+1,n) - N(i,j,k,l-1,n)] \quad (28)$$

with

$$M'(i,j,k+1/2,l,n) = 0.5 c_k [N(i,j,k+1,l,n) + N(i,j,k,l,n)] \quad (29)$$

$$M(i,j,k+1/2,l,n) = \pm \min \left[\frac{N(i,j,k_u,l,n) \Delta(\ln k)}{\Delta t}, |M'(i,j,k+1/2,l,n)| \right] \quad (30)$$

where α is the upstream fraction ($0 \leq \alpha \leq 1$ for $c_x > 0$ and $-1 \leq \alpha \leq 0$ for $c_x < 0$), and u is a suffix indicating the "upstream" bin in k -space (next bin if $c_k > 0$, previous bin if $c_k < 0$). The sign of M in Eq. 30 is the sign of M' .

The first order upstream scheme used in the propagation in x -space assures stable behavior of the propagation module for a suitably chosen upstream fraction α . The stability of the propagation is governed by the spacial resolution of the action density and by the magnitude

of the source term. Since the diffusion terms reduce the accuracy of the propagation module it is best to keep the upstream fraction α as small as possible. We have implemented the expression suggested by Tolman [1991] for the upstream fraction:

$$|\alpha| = \max [\alpha_c, \alpha_{\min}],$$

$$\alpha_c = \min \left[1, 0.10 + 3.75 \frac{S_{in}(k, \theta) \Delta x}{F(k, \theta) c_g} \right] \quad (31)$$

where α_{\min} is chosen large enough to stabilize the source free propagation.

The propagation in k -space incorporates an upstream limited flux scheme. In this method the possibility of generating negative action is removed by requiring that the flux out of a bin in a single time step does not exceed the total action within the bin. For nearly all spectral and spatial bins the flux limitation will normally not be reached and M and M' will be equal. In this case, Eq. (27) reduces to the normal formulation of the Crank-Nickolson scheme. Since k varies over several decades we have chosen an exponential k -grid for better sampling of the lower wavenumbers (frequencies):

$$k_k = k_1 \left[\frac{k_N}{k_1} \right]^{\left(\frac{k-1}{N-1} \right)} = \frac{2\pi}{\lambda_{\max}} \left[\frac{\lambda_{\max}}{\lambda_{\min}} \right]^{\left(\frac{k-1}{N-1} \right)}, \quad k = 1, 2, 3, \dots, N \quad (32)$$

The logarithm of this k -grid is uniformly spaced. Thus, the central two point numerical approximation is appropriate for the k -derivative provided we write it as

$$\frac{\partial}{\partial k} \rightarrow \frac{1}{k} \frac{\partial}{\partial \ln k} \quad (33)$$

This logarithmic form is used in the expression for L_k (Eq. 27).

The propagating in θ -space (Eq. 28) is unaltered from the normal Crank-Nickolson derivative formula. To stabilize propagation in this dimension we have used the conservative

elimination procedure. This amounts to setting all bins with negative action to zero while preserving the sum:

$$N(k) = \int_0^{2\pi} N(k, \theta) d\theta . \quad (34)$$

In this scheme all negative action for a given k -point is removed first; then the action density for all directions θ is multiplied by a constant term to conserve $N(k)$.

For boundary land points we implemented the angle derivative upstream scheme described by Tolman [1991]. In most instances, however, we have been working in patches of the ocean where no land points exist. In these cases an absorbing boundary is used where the action at boundary points is set equal to the action at adjacent interior points at each time step.

At the boundaries in the wavenumber domain we assume that the asymptotic behavior of the spectrum follows that of an assumed equilibrium spectrum N_o . The action density at the upper boundary k -points is generated from the action density at adjacent interior frequencies by

$$N(k) = \frac{N(k_c)}{N_o(k_c)} N_o(k) , \quad k > k_c \quad (35)$$

where k_c is a user supplied upper cutoff wavenumber which depends on the time step and resolution. At the lowest k -point where the action density is rapidly approaching zero the action density spectrum is simply set identically to the equilibrium spectrum.

After the propagation step is complete the source term is included by integrating the following reduced version of the action density equation:

$$\frac{\partial N}{\partial t} = S. \quad (36)$$

The integration is performed using a simple Euler method which gives the updated action density N_{new} by the formula:

$$N_{new} = N_{old} + S \Delta t. \quad (37)$$

Here N_{old} is the action density output from the propagation module (i.e. without the source). Any negative action that results from the integration of the source term at every time step is simply eliminated by setting the action density in that bin to zero. The time step is chosen small enough to satisfy the Courant conditions, $\Delta t < \Delta x_i / c_i$, for each dimension, $\{x_i\} = \{x, y, k, \theta\}$. In practice, the spectral grid is chosen fine enough so that the upper limit on Δt is constrained by the Courant condition in the spacial domain.

Updating the action density at each time step involves a call to the propagation module and then to the source integrator module. The procedure is illustrated in Fig. 1.

4. Testing

The Crank-Nickolson/predictor-corrector propagation scheme has been thoroughly tested previously by Tolman. Our code was checked against Tolman's WAVEWATCH results for each of the compatible test cases presented in his thesis. The results for propagation in x -space and θ -space were identical in appearance to Tolman's results. The propagation in k -space could not be checked against WAVEWATCH which is implemented in the frequency domain rather than wavenumber. However, internal tests of the k -propagation were made by comparing the limited flux scheme to several other forms of the numeric derivative.

In addition, our model was tested against the time-independent environmental research institute of Michigan (ERIM) ocean wave model (EOM). The EOM solves for the equilibrium

action density spectrum for a given steady state current field. The comparisons were done using the one dimensional steady current field of the form:

$$u(x) = u_o \operatorname{sech}^2(x/\delta) \quad (38)$$

which is a stationary soliton-like current which goes to zero at the boundaries $x \rightarrow \mp \infty$. The parameters u_o and δ were chosen to be 0.1 m/s and 20 m. A plot of the current is shown in Fig. 2.

To estimate the changes in the wind waves near the soliton we have used the Hughes form for the source function with β given by

$$\beta = \frac{0.04}{\omega_o} k^2 u_*^2 \left| \cos\left(\frac{\theta - \theta_w}{2}\right) \right|, \quad (39)$$

where u_* is the friction velocity, and θ_w is the wind direction which we take to be zero. The equilibrium spectrum used in the source was the composite spectrum suggested by Bjerkaas and Riedel [1979] which is given in appendix A. The wind direction was along $+x$ with a speed of 5 m/s. A uniform 95 point grid with $\Delta x = 4$ m was used for the mesh along x . The radial wavenumber mesh is computed with Eq. (32) using 82 k -points, with $\lambda_{\min} = 0.001$ m, and $\lambda_{\max} = 50$ m. The angular spectral mesh is uniform with $\Delta\theta = 10^\circ$ (36 angles).

Before the action density equation can be solved it is necessary to provide appropriate boundary conditions for each of the five dimensions. The simulation was started by applying the equilibrium spectrum to all 95 points along x , although any other initial conditions should in principle produce the same equilibrium result. On subsequent time steps only the boundary x -points were set by applying an absorbing boundary condition as discussed previously. The boundaries in the spectral domain were set according to Eq. (35) with $k_c = 2\pi/(0.005 \text{ m})$.

To examine changes in the action density we have defined a fractional difference spectrum R as follows:

$$R(x, k, \theta) = \frac{N(x, k, \theta) - N_o(k, \theta)}{N_o(k, \theta_w)} \quad (40)$$

where θ_w is the wind direction. The time development of R as a function of position x is shown for wavelengths ranging from 1 cm to 15 m in Fig. 3. The solid line in each plot is the function R at time $t=250$ s, while the dotted lines are snapshots of R at previous times separated by 50 s intervals. Apparent in the plots are several transients which have mostly propagated out of the plot window by the maximum time (250 s). Equilibration rates are a function of wavelength, but all wavelengths appear to have reached equilibrium by 250 s. We find that wavelengths near the center of the spectrum, $\lambda \approx 1$ m to 2 m, are most strongly perturbed by the current field. The functional form of the plots are consistent with the rule that longer waves are governed by the current amplitude, while shorter waves are governed by the current gradient. These limiting forms are easily derived from the action density equation (9,12, also see Lyzenga, [1991]), which for small currents, and current gradients (and thus for $R \ll 1$) leads to the approximations

$$R \rightarrow \begin{cases} \frac{\eta}{\beta} \frac{\partial u}{\partial x}, & \beta \delta \gg c_x \gg \lambda \frac{\partial u}{\partial x} \quad (\text{short wave refractive limit}), \\ \frac{\eta}{c_{gx}} u, & \beta \delta, u \ll c_{gx} \quad (\text{long wave advective limit}), \end{cases} \quad (41)$$

where η is the dimensionless number,

$$\eta(x, k, \theta) = \frac{k_x}{N_o(k, \theta_w)} \frac{\partial N_o(k, \theta)}{\partial k_x} = \frac{k \cos \theta}{N_o(k, \theta_w)} \left[\cos \theta \frac{\partial N_o(k, \theta)}{\partial k} + \frac{\sin \theta}{k} \frac{\partial N_o(k, \theta)}{\partial \theta} \right], \quad (42)$$

which is negative for wavelengths anywhere in the tail of the spectrum.

A comparison between the NTOW model results and those of the EOM are shown in Fig. 4. The NTOW model results are plotted at time $t=250$ s when the system appears to have reached equilibrium near $x=0$. The comparison between the models is quite good considering the differences in the numerical methods. The positive "bump" which appears in the NTOW

results for 1 m waves and at the edge of the plot for 2 m waves are transients which are propagating out of the plots. The small differences between the results of the two models for the shortest wavelengths are due to differences in the way the tail region of the spectrum is handled.

Figures 5a, b, and c show the full spectrum results at the center of the soliton and at $x = \mp 20$ m for (5a) R using the NTOW model, (5b) R using the EOM, and (5c) the difference between R for the two models. It is clear from these plots that both models give very similar results for the fractional difference spectrum. However, the maximum perturbation of the spectrum for EOM is slightly larger than that for the NTOW model. Still, from Fig. 5c it appears that the maximum fractional difference between the two models is less than 5 % for all regions of the spectrum.

A radar image of the soliton feature was derived from the wave spectrum using the composite scattering model of Wright [1968], which is implemented in a module of the EOM. Radar imagery can be derived using the output wave field from either wave propagation model as input to the EOM radar module. Figure 6 compares the RAR cross section per unit area obtained with the two ocean wave models for X-Band, HH-polarization and an incidence angle of 37° . We find that the maximum cross section variation for the EOM is larger than that for the NTOW model consistent with the larger perturbations in the wave action density found for EOM. Nevertheless, the two models give very similar results for the radar return, especially in the general shape of the curve.

The results for the stationary soliton show good agreement between the EOM and the NTOW model. This suggests that the NTOW model should give satisfactory results in cases where the currents or winds are not steady. In the next section we examine such a case for a current "Rip" formed by the subduction of Gulf Stream water under shelf water.

5. Rip Feature

5.1. Background

During the NRL high-resolution remote sensing experiment real aperture radar (RAR) data was collected over the shelf region off Cape Hatteras. The RAR data show many features which are known to be associated with current structures near the Gulf Stream. However, the precise nature of these features is still unknown. Some of the more obvious mechanisms which could produce these features are, wave current interaction, wave breaking, and surfactant damping or combinations of these effects.

A particularly striking feature seen in the NRL high-resolution RAR data was a meandering line in the region between the Gulf Stream water and the coastal shelf water. The RAR image of the line feature, which has been named a current "Rip" feature, is shown in Fig. 7. The Rip is from 5dB to 20dB above the background and is visible over several kilometers along the shelf. Unfortunately, no accurate measurements of surface currents are available in this region. From measurements of deeper ocean currents and analysis of the RAR data it was estimated that the Rip is advected primarily in a northerly direction at about 0.4 m/s. It is believed that the Rip feature results from wave-current interaction effects associated with surface convergence (downwelling) along a line where Gulf Stream water is subducted under slower shelf water [Mied *et al.*, 1992]. The subduction occurs because the Gulf Stream water is more dense than the shelf water due to its higher salinity.

5.2. Modeling of Rip

Although the RAR intensity has some variation along the Rip, the effect is expected to be predominantly associated with current variations in the direction perpendicular to the feature. We have, therefore, modeled the Rip currents as one dimensional. The form used to describe the currents in the direction perpendicular to the Rip is

$$v(y) = a - b \tanh \left(\frac{y - ct}{\delta} \right). \quad (43)$$

A plot of the current is shown in Fig. 8. The parameters a , b , c , and δ were estimated to be near the values $a=0.5$ m/s, $b = 0.1$ m/s, $c = 0.4$ m/s, and $\delta = 10$ m. However, these values are only approximate since the available current data near the rip is inadequate to determine the current field precisely. For this reason, we have examined the sensitivity of the radar return to variations in these parameters.

The calculations were done using the NTOW model in a coordinate system with x pointing along the Rip (predominantly east) and y perpendicular to the Rip (predominantly north). The grid in the spacial domain along y uses 145 points with a uniform spacing of $\Delta y = 4$ m. The radial wavenumber mesh is computed from Eq. (32) using 62 k -points, with $\lambda_{\min} = 0.001$ m, and $\lambda_{\max} = 50$ m. The angular spectral mesh is uniform with 24 angles ($\Delta\theta = 15^\circ$). The simulation was initiated by applying the equilibrium spectrum N_0 to all points at time $t = 0$. On subsequent time steps N_0 was applied only to boundary points.

To estimate changes in the wind waves near the Rip we have again used the Hughes form with β given by Eq. (39) and the Bjerkaas and Riedel [1979] equilibrium spectrum (see appendix A). The measured wind direction and speed are shown in Fig. 9. From Fig. 9 it follows that over typical equilibration time scales for the Bragg waves and waves of a few meters the wind variation is negligible. At the time the RAR data were obtained the wind was from the South-West at about 3 m/s. In the calculations we use a fixed wind speed of 3 m/s and have also ignored the relative wind speed corrections in the source term since the current speed is small.

Some preliminary calculations for the Rip were also done using the EOM wave propagation model by shifting the coordinate system to the frame centered on the rip. In this frame the currents are steady so that the EOM model is applicable. However, our calculations using the EOM show very poor convergence of the perturbed wave field with grid spacing for

many of the cases considered here. Although the shape of the wave field predicted with the EOM is consistent with NTOW results, the magnitude continued to change significantly for variations in grid spacing, even when the grid spacing was much less than the convergence zone width. Due to its slow convergence, the wave field predictions from the EOM model are not included in this report. Further discussion of this problem is given in appendix B.

5.3. Wave Field Prediction

Figure 10 shows the time development of the \hat{y} -component of the fractional difference spectrum, $R(k, \theta=90^\circ)$, for a number of wavelengths ranging from 1 cm to 10 m. The wind is at 45° toward the north east (*i.e.* $\theta_w=45^\circ$). The different curves for a given wavelength represent the function R at times separated by $\Delta t = 30$ s. The shift in the curves toward the north (higher y) is due to the advection of the Rip with a drift speed of $c = 0.4$ m/s. The general behavior of R as a function of wavelength can be understood from the approximate expressions given in Eq. (42). That is, we find that the shortest waves are governed by the magnitude of the current gradient while the longest waves are governed by the current magnitude. As the waves approach the Rip from the south they are refracted towards the north by the current gradient according to Eq. (10). Longer waves are also shifted to higher frequencies upon entering the slower moving water on the north side. Thus, shorter waves are enhanced near the Rip edge on the north side. The results also show that the shortest waves are affected only very near the vicinity of the convergence front by the current gradient, while longer waves are advected and continue to propagate with a perturbed action density some distance from the Rip on the north side.

Even for a fixed wind direction the angle that the wind makes with the Rip varies since the Rip meanders. We have therefore computed the action density across the Rip for several wind directions. Figure 11 shows the contour and surface plots of R for wind directions towards (11a) 20° , (11b) 45° , and (11c) 70° from the Rip line (x -axis). For each wind direction the plots are shown at locations $y = -20$ m (south side of Rip), $y = 0$ m (center of Rip), and $y = +20$

m (north side of Rip). The largest enhancement of the waves is on the north side and is due to the shift of the waves to shorter wavelengths upon crossing the convergence zone center. This enhancement will be greatest for waves traveling perpendicular to the Rip line. Thus, the peak on the north side is found to be largest for the wind direction $\theta_w = 70^\circ$.

The sensitivity of R to variations in the convergence speed b or width δ is presented in Fig. 12. The spectrum R is shown for the matrix of parameters $b = .1$ m/s, $.2$ m/s, and $.3$ m/s, and $\delta = 10$ m, 20 m, and 30 m for fixed $a (= .5$ m/s), $c (= .4$ m/s), and $\theta_w (= 45^\circ)$. In all cases the general shape of the fractional difference spectrum is very similar to Fig. 11b. However, the magnitude of the enhancement varies with these parameter changes, increasing as the convergence speed, b , increases and decreasing as the convergence zone width δ increases. The sensitivity of R to variations in b appears to be especially strong and nonlinear, growing by threefold, for example, for a doubling of b from $.1$ m/s to $.2$ m/s. However, it is expected that for such large current gradients the Hughes source term may be inappropriate. The results for very large fractional changes should therefore be viewed with some caution.

5.4. Radar Predictions

We have also derived composite scattering model predictions of the RAR imagery for each of the cases involving the Rip discussed above. In these calculations the plane flies parallel to the Rip on the north side as was done in the measured RAR data shown in Fig. 7. The RAR incidence angle at the Rip was near 37° , but we have examined the response of the RAR to variations in this angle. The predicted HH-polarized X-band (12.7 GHz) RAR return for the Rip when the standard Rip parameters ($a = .5$ m/s, $b = .1$ m/s, $c = .4$ m/s, $\delta = 10$ m, $\theta_w = 45^\circ$) and a 37° incidence angle are assumed is shown in Fig. 13. Consistent with the simplest radar models, we find that the shape of the curve looks much like the shape of R for short waves.

Figure 14 shows the dependence of the RAR on wind direction relative to the Rip (14a), convergence speed b for fixed $\delta = 10$ m (14b), and RAR incidence angle (14c). It is found that

the changes in the RAR cross section roughly follow changes in R as the wind direction and convergence speed are varied (14a,b). As in the behavior of R , the RAR cross section is particularly sensitive to changes in the convergence speed, growing nonlinearly with increases in parameter b (Fig. 14b). The largest return is for convergence speed $b = .3$ m/s (with $\delta = 10$ m) where the gain is about 12 dB. This is well within the range of the measured gain of 5 dB to 20 dB. The dependence on incidence angle shows a downward trend in the return near 37° incidence. The falloff in the curve in Fig. 13c near zero incidence is due to a breakdown in the composite scattering model for very small incidence angles and is not realistic.

A more complete view of the dependence of the HH-RAR return on variations of parameters b , and δ is shown in Fig. 15. Here we show the maximum gain in the RAR return for the 3X3 matrix of cases with different b and δ values and a fixed incidence angle of 37° and wind direction of 45° . As expected the largest gain in cross section (about 12 dB) is obtained for the smallest δ and largest b considered. The dependence on b is strong as discussed previously. However, the sensitivity of the RAR to changes in δ is relatively weak. In general, our results for the maximum radar return in the Rip appear to be somewhat less than those observed in the RAR data. This is not surprising since, among other factors, we have neglected wave breaking, which is expected to be important in the Rip region, especially for the higher convergence speeds. Surfactant effects are also not included in our simulations, however, preliminary studies of expected surfactant effects suggest these will be weak near the Rip, but could be significant away from the Rip, reducing the amplitude of waves shorter than about 1 m.

6. Summary

A time dependent ocean wave (NTOW) model has been developed to simulate the propagation of waves over current and depth structures. The model solves the action density conservation equation using a finite step method. Comparisons of the model were made against Tolman's WAVEWATCH model and the ERIM Ocean Model (EOM) to determine the reliability of the propagation scheme. Agreement between the various models was found to be satisfactory.

We have used the NTOW model along with the composite scattering model to make predictions of the radar return from a current Rip and compared our results with measured RAR data. Our predictions of the RAR cross section for the current Rip are found to be consistent with measurement, but generally show smaller variation. However, the effects of whitecapping and surfactants have not been included in our modeling. It is expected that including these effects will produce better agreement with experiment. It is hoped that these effects can be included in future work. Also, more realistic source terms are being implemented.

Acknowledgments.

We would like to thank H. Tolman for describing his WAVEWATCH program to us in detail in the initial stages of the development of NTOW. We are also indebted to A. Cooper for many valuable discussions and continuing collaborations with us on issues related the EOM code and our modeling efforts. We thank F. Askari for providing us with the RAR image of the Rip. G. Marmorino and C. Trump were helpful in supplying preliminary results associated with Rip current modeling.

REFERENCES

- Bjerkaas, A.W. and F.W. Riedel, 1979: Proposed model for the elevation spectrum of a wind-roughened surface. Rep. TG-1328, 31 pp., Appl. Phys. Lab., Johns Hopkins Univ., Laurel, Md.
- Bretherton, F.P. and C.J.R. Garrett, 1968: Wave trains in inhomogeneous moving media. Proc.R. Soc. (A) **302**, 539.
- Hasselmann, K., 1962: On the non-linear energy transfer in a gravity-wave spectrum. J. Fluid Mech., **12**, 481
- Hasselmann, K., 1968: Weak-interaction theory of ocean waves. Basic developments in fluid Mech, **2**, M. Holt (ed.), Academic Press, New York, 117.
- Hughes, B.A., 1978: The effect of internal waves on surface wind waves, 2, Theoretical analysis. J. Geophys. Res., **83**, 455.
- Lyzenga, D.R., 1991: Interaction of short surface and electromagnetic waves with ocean fronts. J. Geophys. Res. **96**, 10765.
- Mied, R.P., F. Askari, G.O. Marmorino, G.R. Valenzuela, and D.B. Trizna, 1992: High resolution remote sensing. 1992 NRL Review, pp. 181-183.
- Phillips, O.M., 1957: On the generation of waves by turbulent wind. J. Fluid Mech. **2**, 417.
- Plant, W.J., 1982: A relationship between wind stress and wave slope. J. Geophys. Res. **87**(c3), 1961.

Tolman, H.L., 1991: A third generation model for wind waves on slowly varying, unsteady and inhomogeneous depths and currents, *J. Phys. Oceanogr.*, **21**, 782-797

van Gastel, K., 1987: Nonlinear interactions of gravity-capillary waves: Lagrangian theory and effects on the spectrum. *J. Fluid Mech.* **182**, 499

Valenzuela, G.R., and M.B. Laing, 1972: Nonlinear energy transfer in gravity-capillary wave spectra, with applications. *J. Fluid Mech.* **54**, 507.

Valenzuela, G.R. *et al.*, 1991: The July 1990 Gulf Stream experiment. *IGARSS 1991 Proc.*, vol. I, 119, Espoo, Finland.

Whitham, G.B., 1967: Variational methods and application to water waves. *Proc. R. Soc. (A)* **299**, 6.

Wright, J.W., 1968: A new model for sea clutter. *IEEE Trans. Antennas Propag.*, **AP-14**, 749.

APPENDIX A: Equilibrium Spectrum

The equilibrium action spectral density $N_o(k, \theta)$ is related to the equilibrium variance density spectrum $F_o(k, \theta)$ by

$$N_o(k, \theta) = \frac{\rho \omega_o}{k} F_o(k, \theta) \quad (\text{A1})$$

The spectrum $F_o(k, \theta)$ is that proposed by *Bjerkaas and Riedel* [1979] which for low or moderate wind speeds ($u_w < 10$ m/s) is written as:

$$F_o(k, \theta) = E_o(k) G_o(\theta), \quad (\text{A2})$$

where

$$G_o(\theta) = \frac{4}{3\pi} \cos^4 \left[\frac{\theta - \theta_w}{2} \right] \quad (\text{A3})$$

and

$$E_o(k) = \begin{cases} E_{PM}(k), & k < k_1 \\ E_K(k), & k_1 \leq k < k_2 \\ E_{MH}(k), & k_2 \leq k < k_3 \\ E_V(k), & k \geq k_3 \end{cases} \quad (\text{A4})$$

where $E_{PM}(k)$ is the *Pierson-Moskowitz* spectrum:

$$E_{PM}(k) = \frac{0.0081}{2k^4} \exp \left[\frac{0.74g^2}{(30u_*')^4 k^2} \right] \quad (\text{A5})$$

$E_K(k)$ is the *Kitaigorodskii* spectrum:

$$E_K(k) = \frac{0.4375 (2\pi)^{p-1} \left[1 + \frac{3k^2}{k_m^2} \right]}{g^{(p-1)/2} k \left[k_2 + \frac{k_2^3}{k_m^2} \right]^{(p-4)/2} \left[k + \frac{k^3}{k_m^2} \right]^{5/2}}, \quad (A6)$$

where k_m is taken to be $k_m = 363 \text{ m}^{-1}$, and $p = 5 - \text{Log}_{10} u_*$.

$E_{MH}(k)$ is the *Mitsuyasu-Honda* spectrum:

$$E_{MH}(k) = \frac{.4375 (2\pi)^{p-1} \left[1 + \frac{3k^2}{k_m^2} \right]}{k g^{(p-1)/2} \left[k + \frac{k^3}{k_m^2} \right]^{(p+1)/2}} \quad (A7)$$

and $E_V(k)$ is the *viscous damping* spectrum

$$E_V(k) = \frac{0.0001473 (u_* k_m^2)^3}{k^{10}}. \quad (A8)$$

The values of k_1 , k_2 , and k_3 satisfy the matching conditions:

$$\begin{aligned} E_{PM}(k_1) &= E_K(k_1), \\ E_K(k_2) &= E_{MH}(k_2), \\ E_{MH}(k_3) &= E_V(k_3). \end{aligned} \quad (A9)$$

This fixes k_1 and k_3 to values which are functions of u_* . However, k_2 is arbitrary and was set to the value $k_2 = 263.86 \text{ m}^{-1}$. The friction velocity u_* is related to the wind speed u_w at height h above the sea surface through the formula

$$u_w = \frac{u_*}{0.4} \ln \left[\frac{h}{Z_o} \right], \quad (A10)$$

where

$$Z_o = \frac{6.84 \times 10^{-5}}{u_*} + 4.28 \times 10^{-3} u_*^2 - 4.43 \times 10^{-4} \quad (\text{A11})$$

Typically, h is chosen to be 19.5 m in which case this reduces approximately to (for $u_w \sim 5$ m/s)

$$u_w(h=19.5\text{m}) \approx 30 u_* . \quad (\text{A12})$$

A plot of the equilibrium variance density spectrum $F_o(k, \theta)$ is shown in Fig. A1.

APPENDIX B: Convergence of Wave Models with Grid Spacing

Wave models of a convergent flow with current speeds near that of the Rip frequently predict very large enhancements in the wave field when a Plant-Hughes source is used. We have used two models to make these predictions: the ERIM Ocean-wave Model (EOM) RSLWAVE, and the NRL Time dependent Ocean Wave (NTOW) model. Our calculations have consistently found some disagreement between these two models, especially for the larger convergence speeds. RSLWAVE always produces larger enhancements than NTOW, but the differences between the models are negligible when the fractional difference spectrum, R , is small:

$$R(x,k) \equiv \frac{N(x,k) - N_o(k)}{N_o(k)} \ll 1, \quad (\text{B1})$$

where N_o is the equilibrium spectrum. The disagreement between the models grows substantially, however, as R increases (for $\Delta x = 4$ m). For example, for the largest Rip velocity gradients considered, 0.03 s^{-1} , RSLWAVE predicts an R value of around 16, while NTOW predicts 10.2 - a dramatic difference!

From some preliminary testing, the source of this discrepancy between the models is apparently due to the high sensitivity of RSLWAVE to the choice of grid spacing Δx . For any realistic modeling the grid spacing should be kept small compared to the width of the convergence zone δ . But, it is found that the predictions for R using RSLWAVE vary appreciably with changes in Δx even when this condition is well satisfied. Figure B1 shows a plot of the peak value of R as a function of $\delta/\Delta x$ at a point 10 m on the north side of the Rip. The Rip current is modeled as

$$u(x) = 0.1 - 0.3 \tanh(x/\delta) \quad (\text{B2})$$

with $\delta = 10$ m. We see that convergence in the NTOW model is reached around $\Delta x = 4$ m, whereas RSLWAVE is still changing significantly in this region.

The reason for the slow convergence of RSLWAVE is not related to round off errors. Doubling the precision made no change in the results. The cause must therefore be related to the propagation scheme used in the models. RSLWAVE uses a forward propagation scheme in which spectral derivatives of the action density are connected in the discrete relation to spacial derivatives at different points in phase space. Thus a correlation between spacial resolution and spectral variations is made possible, and should grow worse with increasing Δx . In NTOW all spectral and spacial derivatives are central derivatives about the same point in phase space in the discrete expression of the action density equation. This minimizes the possibility of any correlation between the spectral changes and the grid resolutions. In general RSLWAVE tends to produce larger perturbations in the wave field due to current structures even when well conveyed. This may be related to the use of a diffusion term in NTOW which tends to smooth rapid variations in the action.

Of course, for the cases considered here it should be realized that the Plant-Hughes form may be inappropriate. In any case, a user of these models should be aware of these discrepancies.

TIME ITERATION LOOP

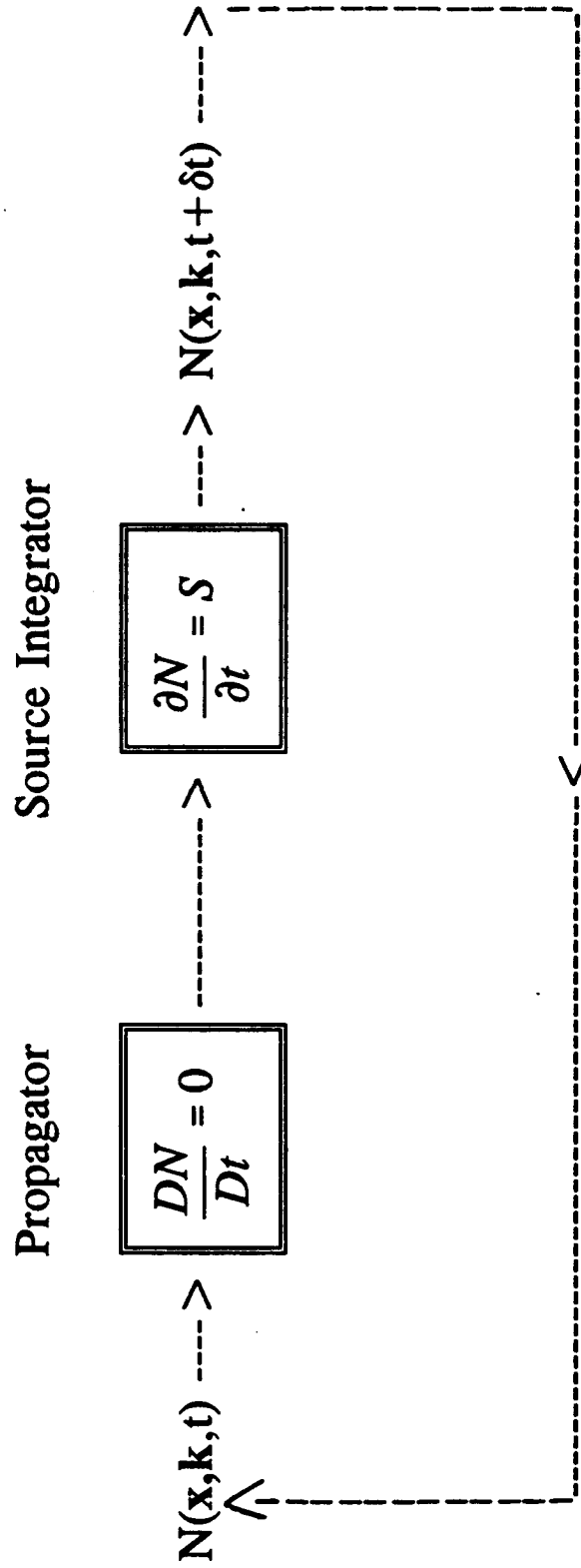


Fig. 1. Time loop diagram for the NTOW model.

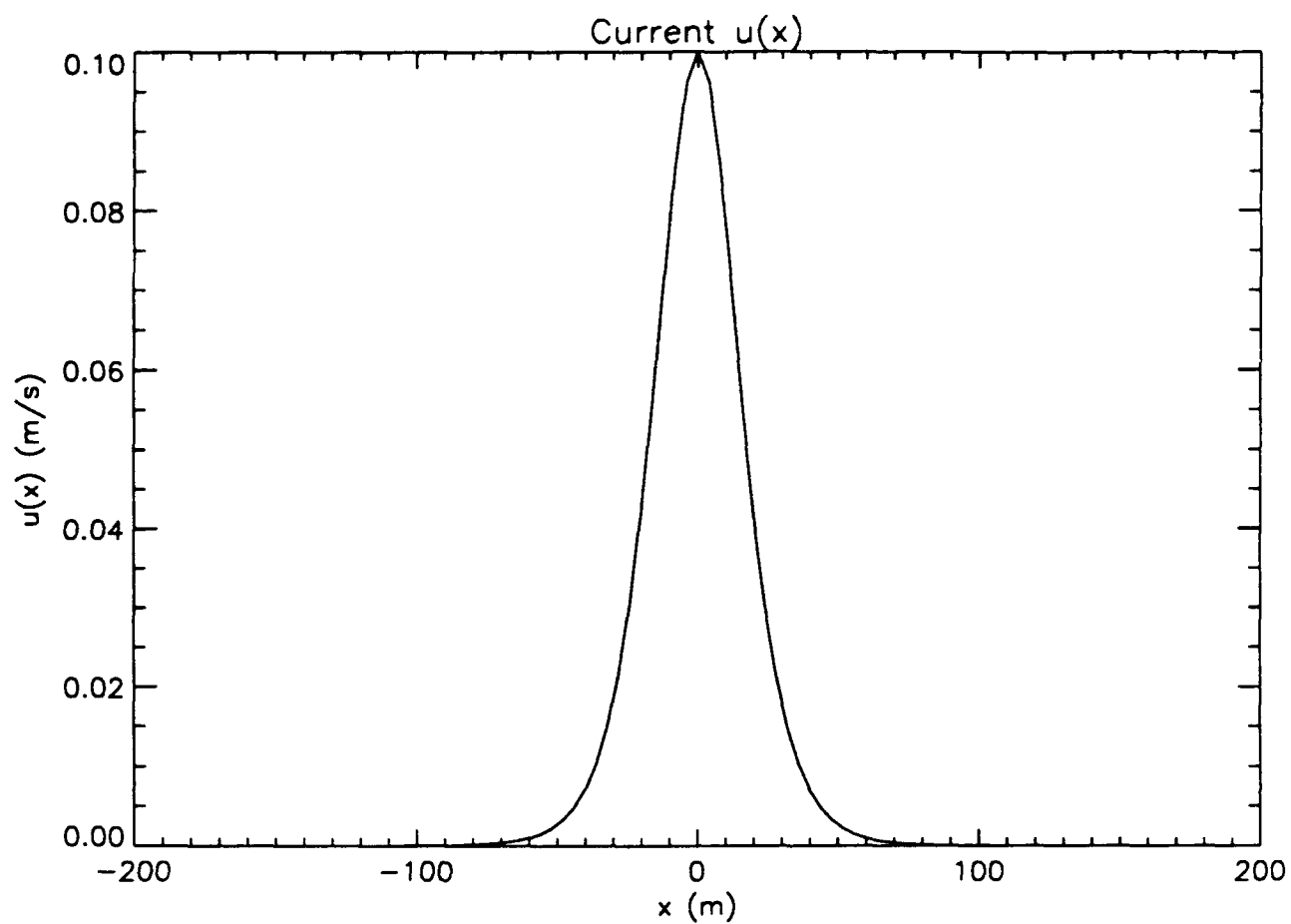


Fig. 2. Plot of stationary soliton current field, $u(x)=0.1 \operatorname{sech}^2(x/20)$, in MKS units.

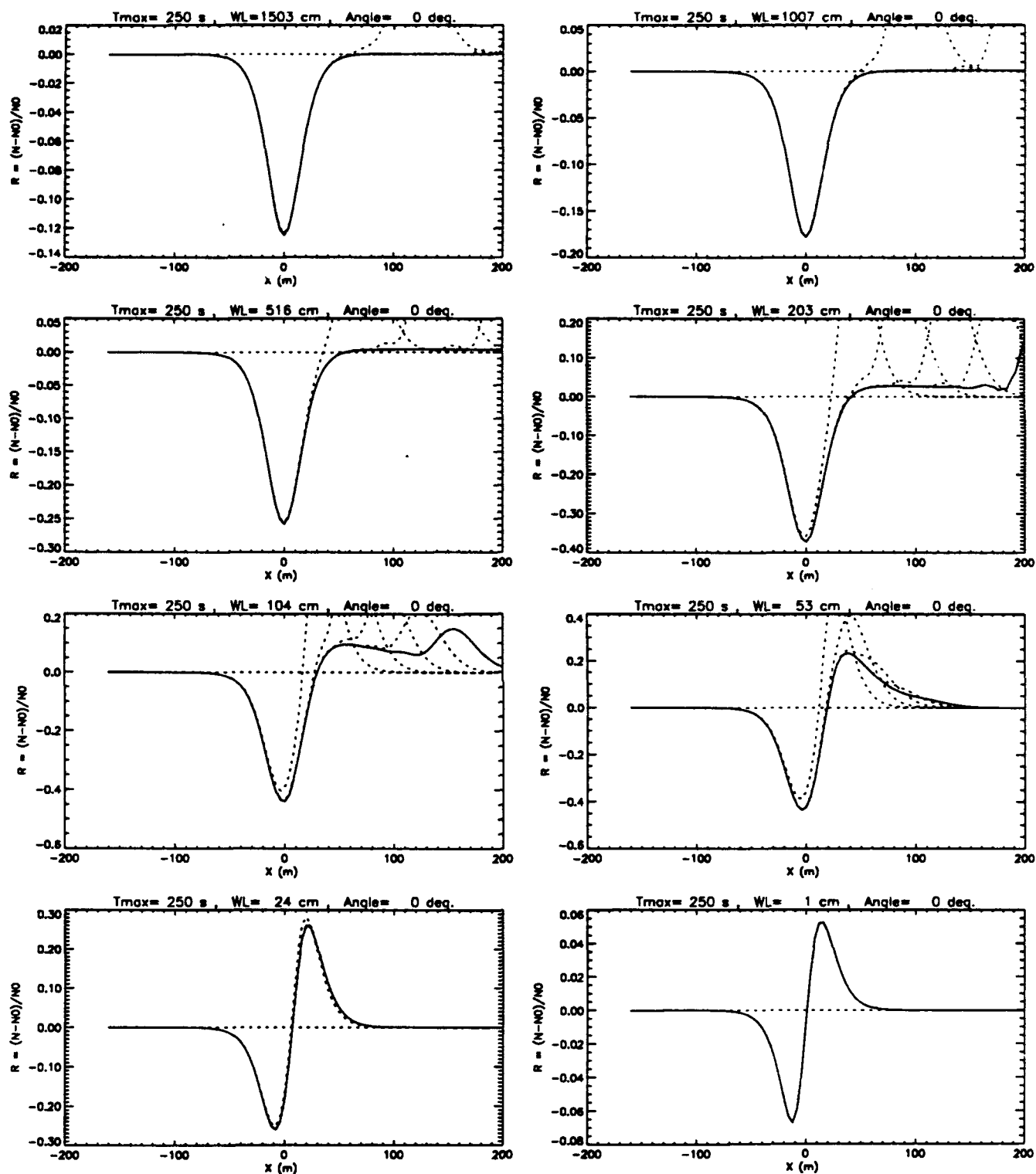


Fig. 3. Time development of fractional difference spectrum $R(k, \theta=0^\circ)$ vs x for several wavelengths (WL values). The solid line is R at time $t=250$ s. Dotted lines are plots of R for previous times separated by 50 s.

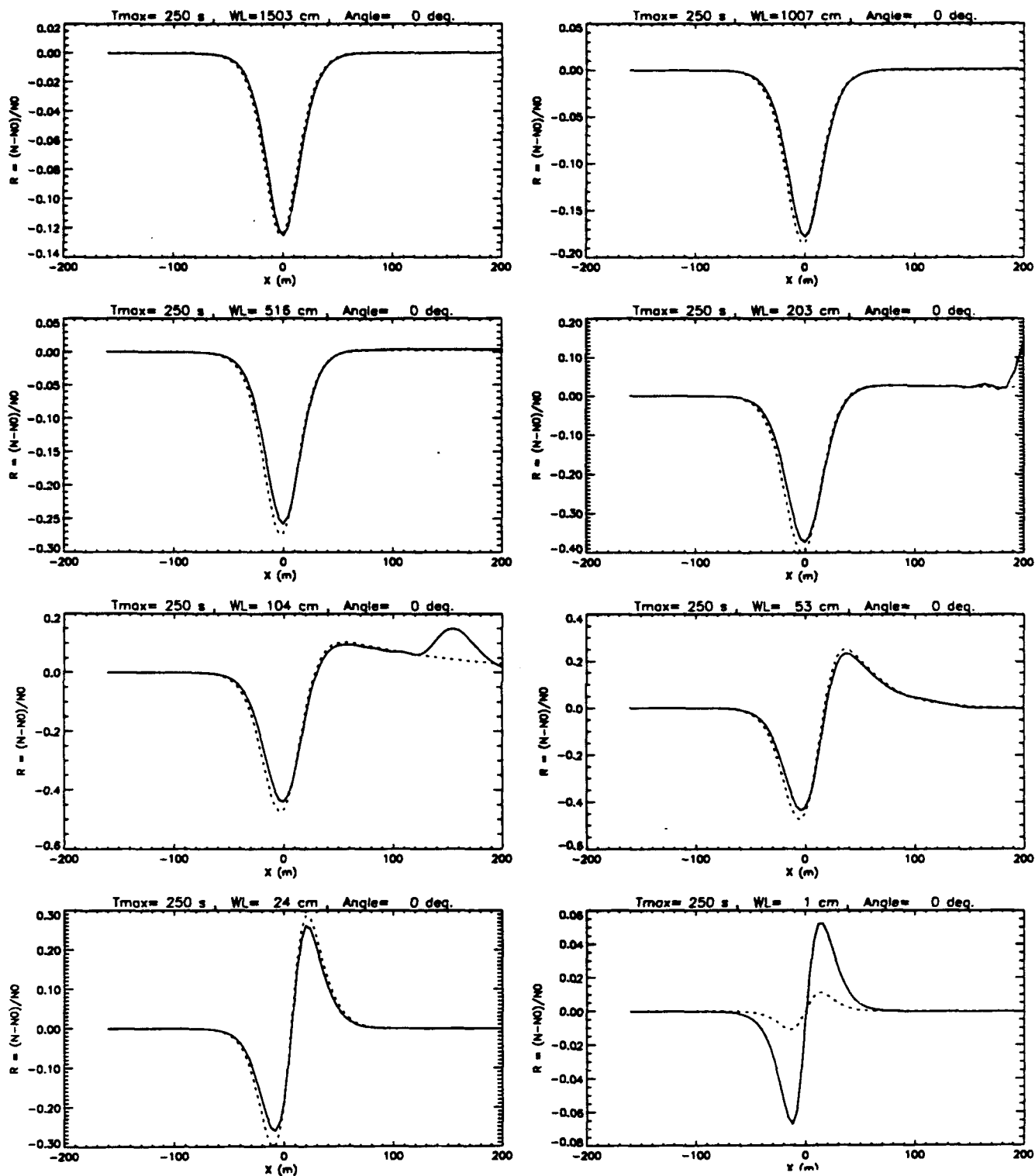


Fig. 4. Comparison between EOM (dotted lines) and the NTOW model (solid lines) results for the fractional difference spectrum $R(k, \theta=0^\circ)$ vs x at several wavelengths (WL's).

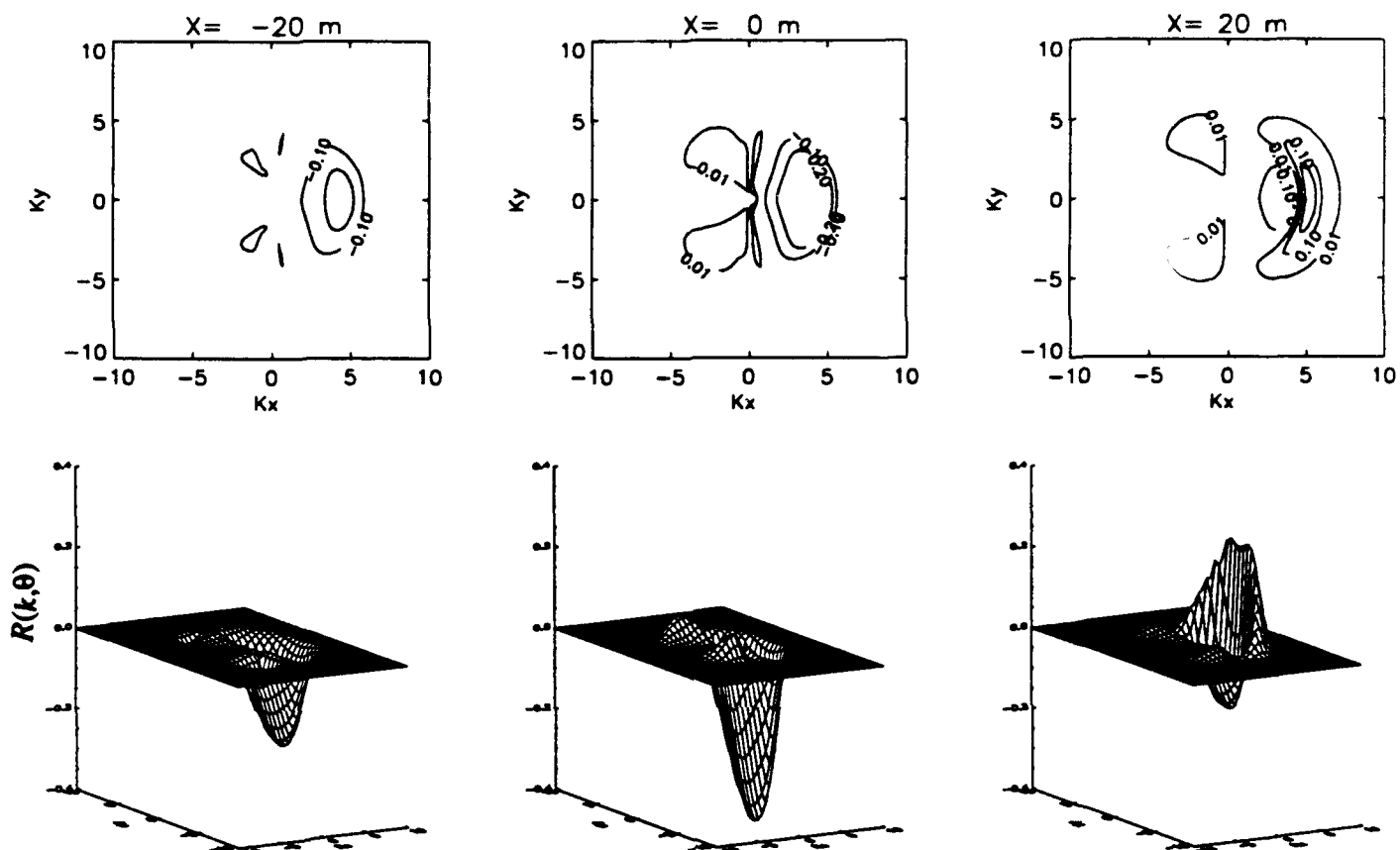


Fig. 5a. NTOW model contour and surface plots of equilibrium fractional difference spectrum $R(k,\theta)$ for the soliton at $x = -20$ m, $x = 0$ m (center of soliton), and $x = 20$ m. The axes are the dimensionless numbers $Kx = \ln(k/k_{\max})\cos\theta$, and $Ky = \ln(k/k_{\max})\sin\theta$, where $k_{\max} = (2\pi/.001) \text{ m}^{-1}$.

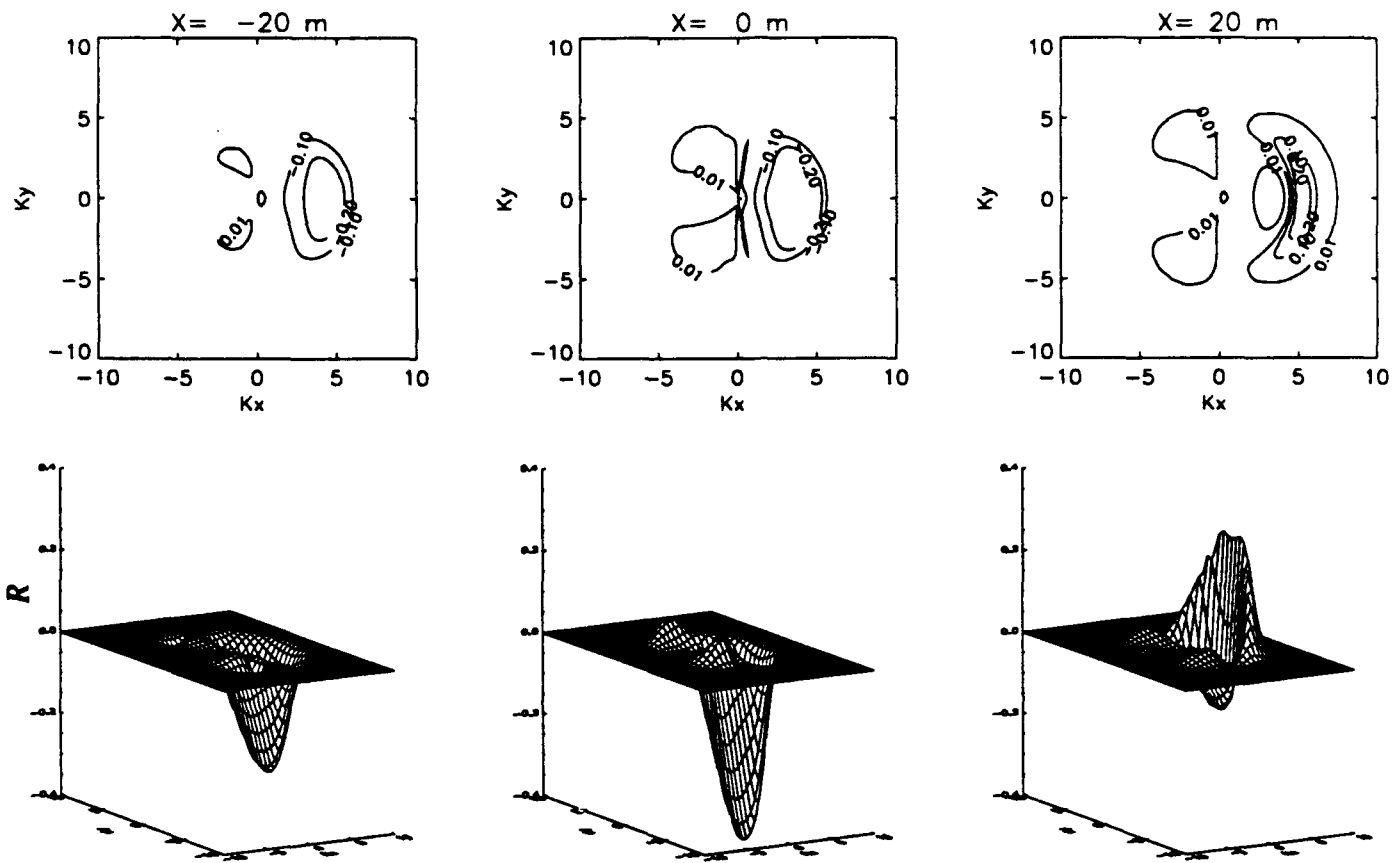


Fig. 5b. EOM contour and surface plots of fractional difference spectrum $R(k, \theta)$ for the soliton at $x = -20$ m, $x = 0$ m (center of soliton), and $x = 20$ m. The axes are the dimensionless numbers $K_x = \ln(k/k_{\max})\cos\theta$, and $K_y = \ln(k/k_{\max})\sin\theta$, where $k_{\max} = (2\pi/0.001) \text{ m}^{-1}$.

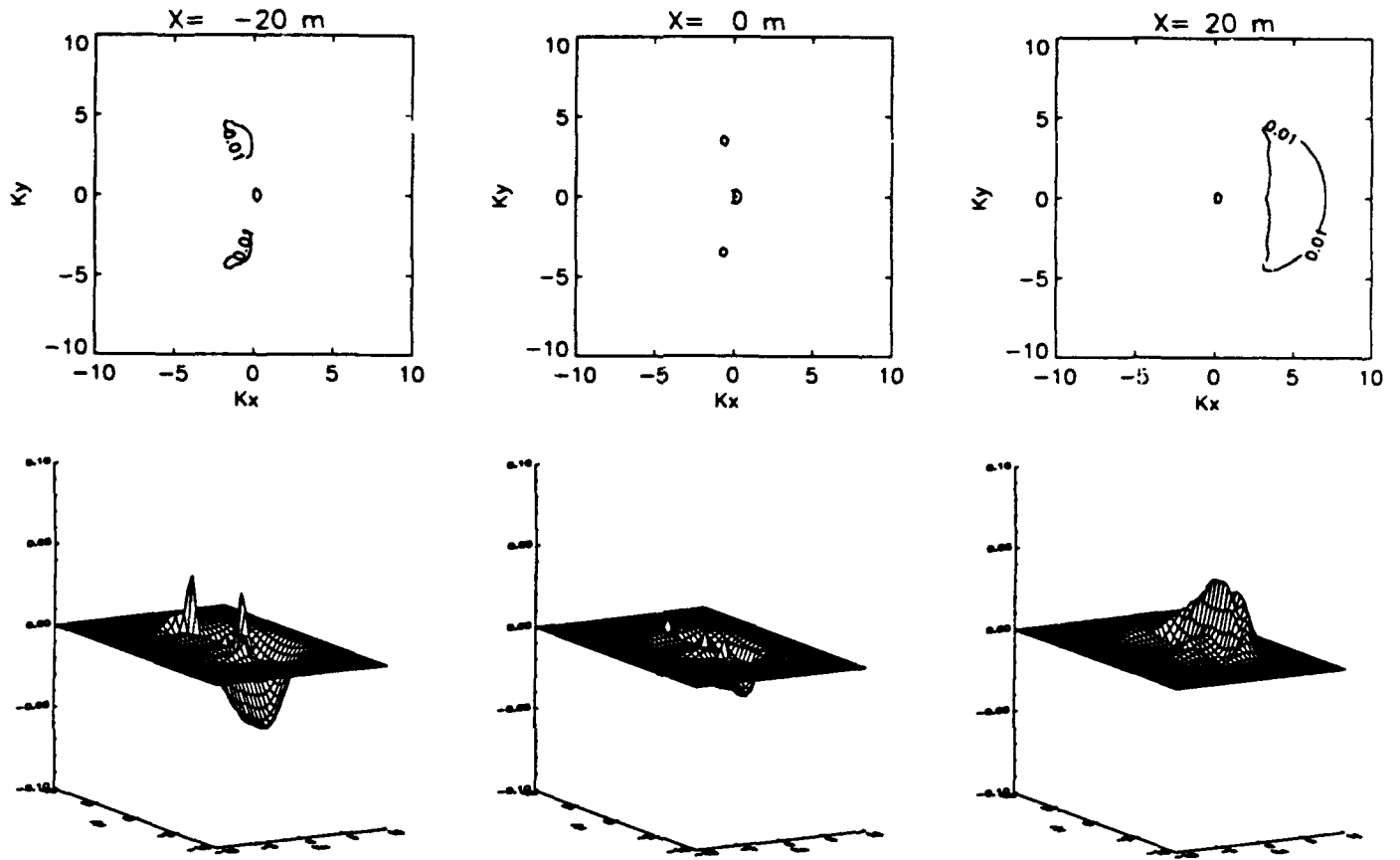


Fig. 5c. Contour and surface plots of the spectrum $(N_{\text{EOM}} - N_{\text{NTOW}})/N_0$ at equilibrium for the soliton at $x = -20$ m, $x = 0$ m (center of soliton), and $x = 20$ m. The axes are the dimensionless numbers $Kx = \ln(k/k_{\text{max}})\cos\theta$, and $Ky = \ln(k/k_{\text{max}})\sin\theta$, where $k_{\text{max}} = (2\pi/0.01) \text{ m}^{-1}$.

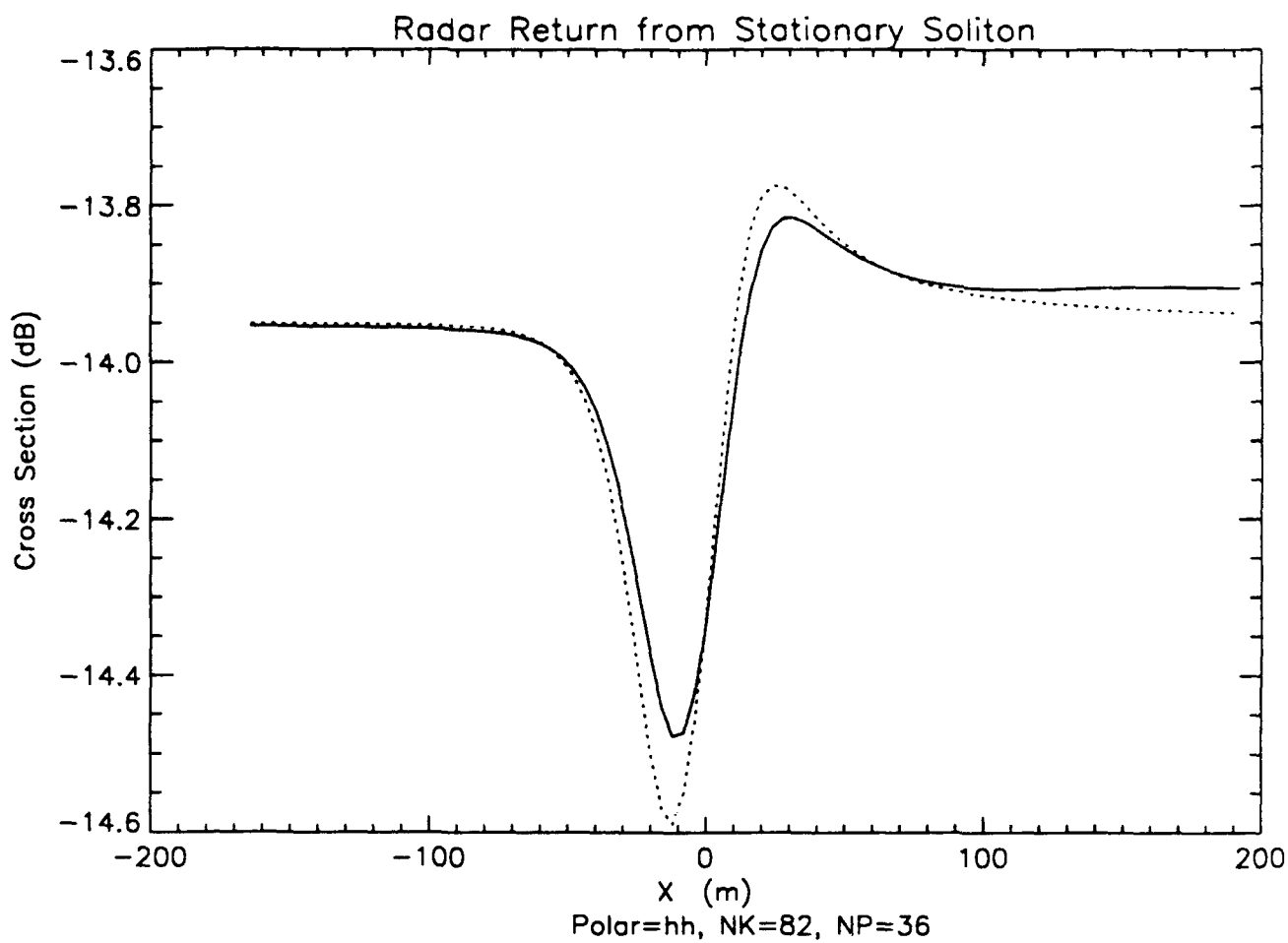


Fig. 6. Plot of X-Band, HH-polarization radar cross section for the soliton using the EOM (dotted line) and the NTOW model (solid line). The incidence angle is 37° .

HI RES ARI September 17, 1991 Pass 27

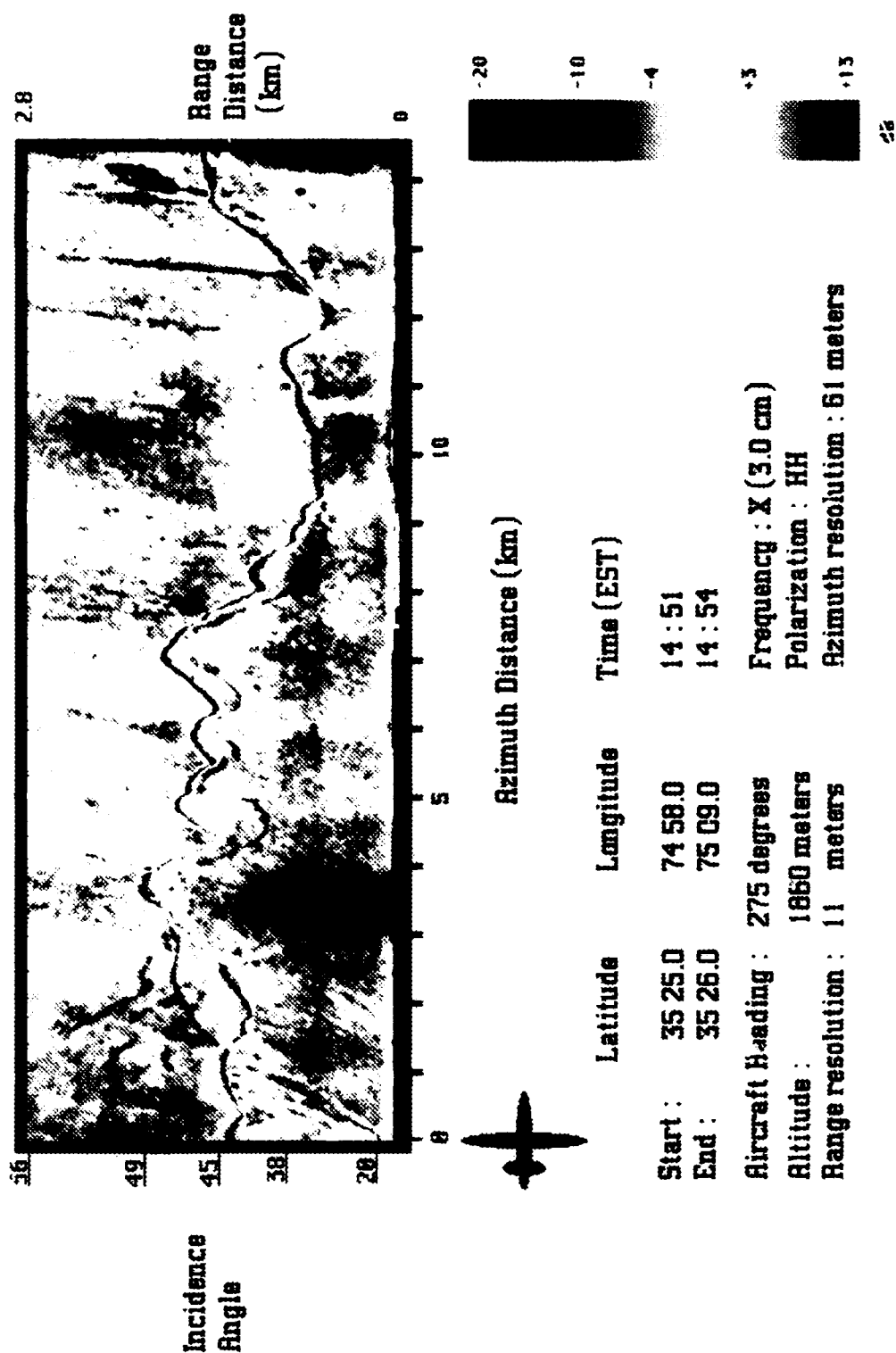


Fig. 7. RAR image of "Rip" feature off Cape Hatteras taken by F. Askari during NRI, high-resolution remote sensing experiment.

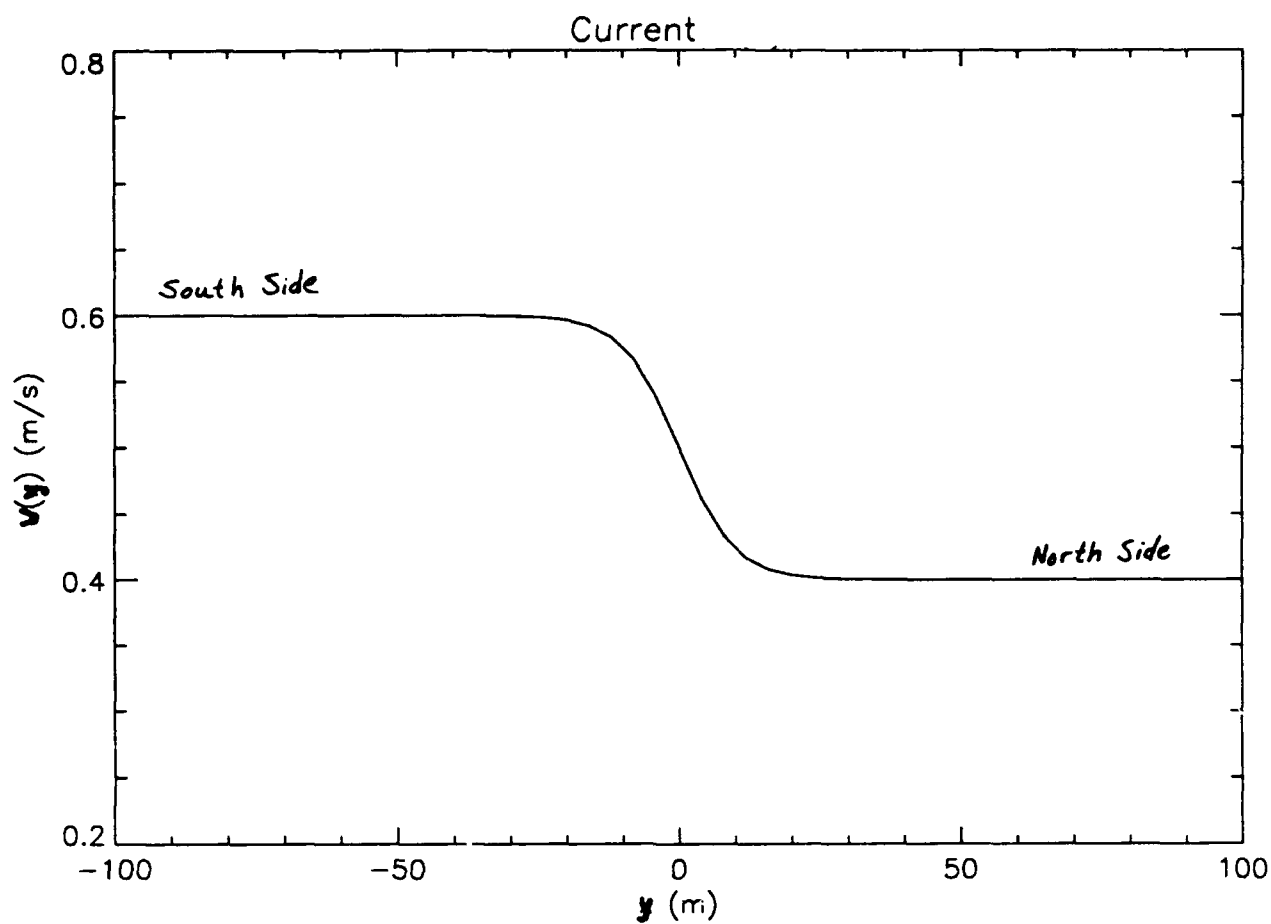


Fig. 8. Initial Rip current for standard parameters: $a = .5$ m/s, $b = .1$ m/s, $\delta = 10$ m in Eq. 43.

WIND MEASUREMENTS NEAR RIP FEATURE

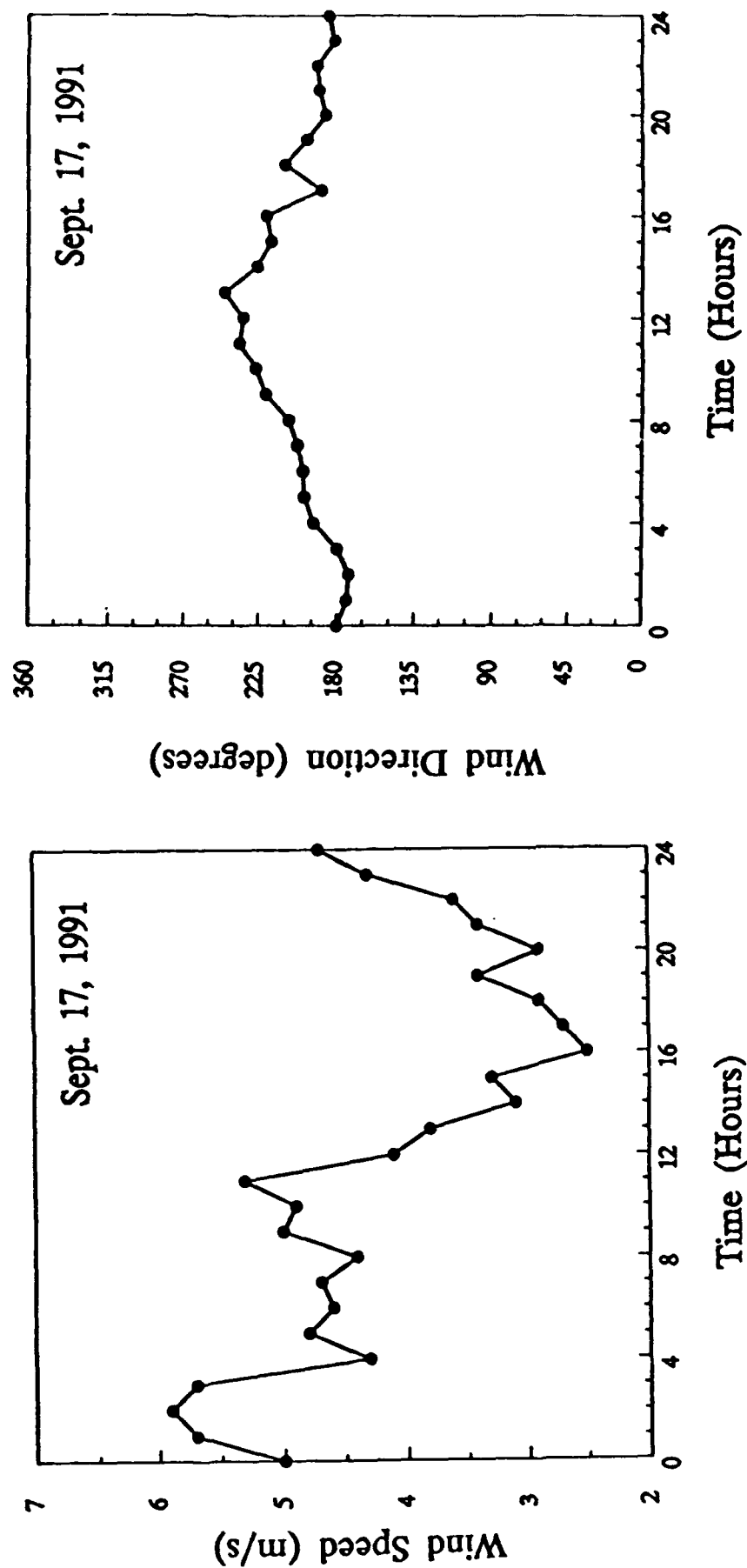


Fig. 9. Wind speed and direction near Rip on day RAR data was collected.

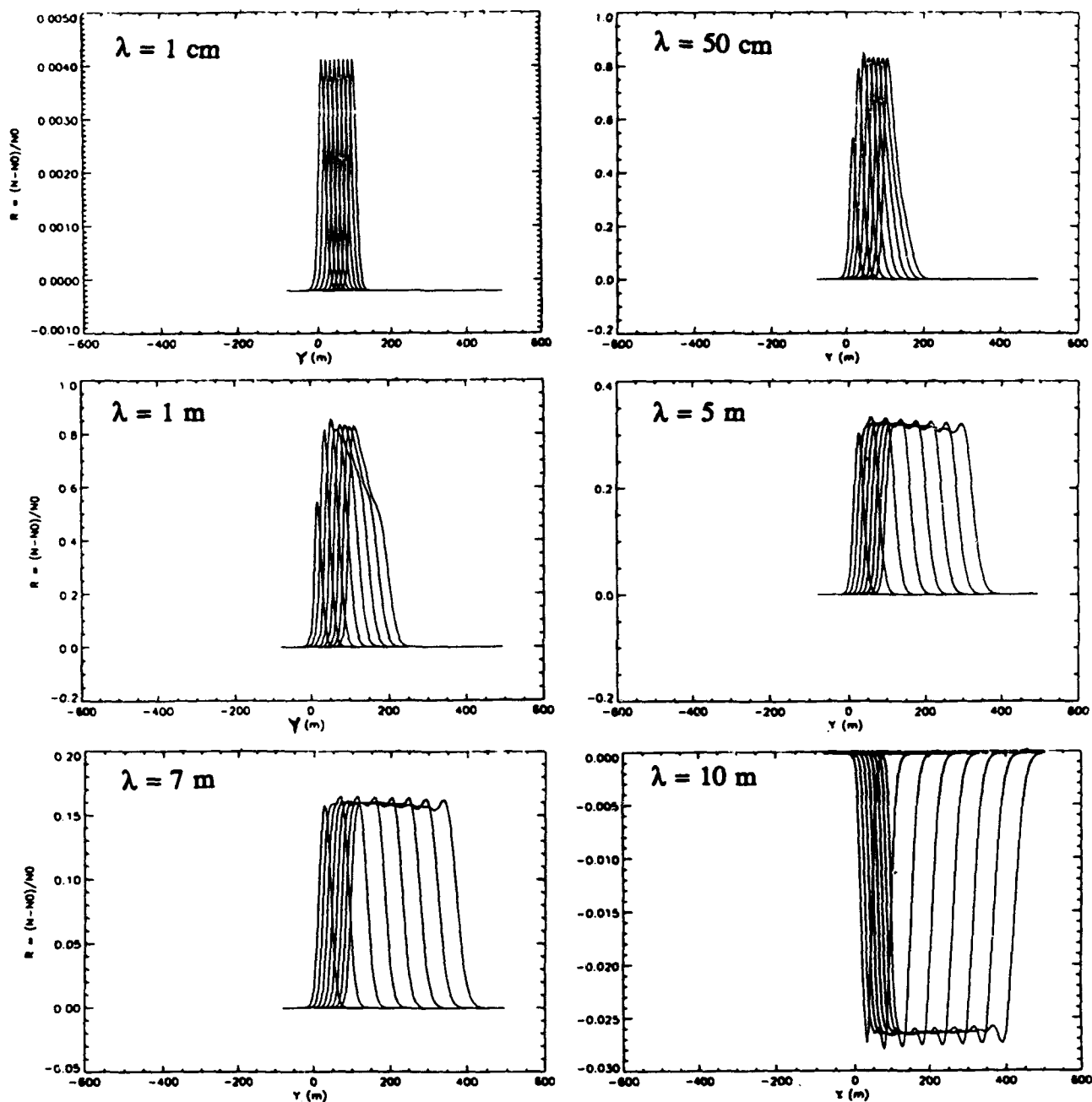


Fig. 10. Development of fractional difference spectrum $R(k, \theta=90^\circ)$ for 1 cm, 50 cm, 1 m, 5 m, 7 m, and 10 m, waves propagating across a current "Rip" (parameters $a = 0.5$ m/s, $b = 0.1$ m/s, $c = 0.4$ m/s, and $\delta = 10$ m). The wind direction is $\theta_w = 45^\circ$ toward NE. The time interval between the curves on each plot is $\Delta t = 30$ s. Notice that the effect on the shortest waves is small and very localized to the Rip region. For medium size waves (≈ 1 m) the effect is larger and less localized. For still longer waves the effect is reduced but extends well into the north side region ($y > 0$) of the Rip.

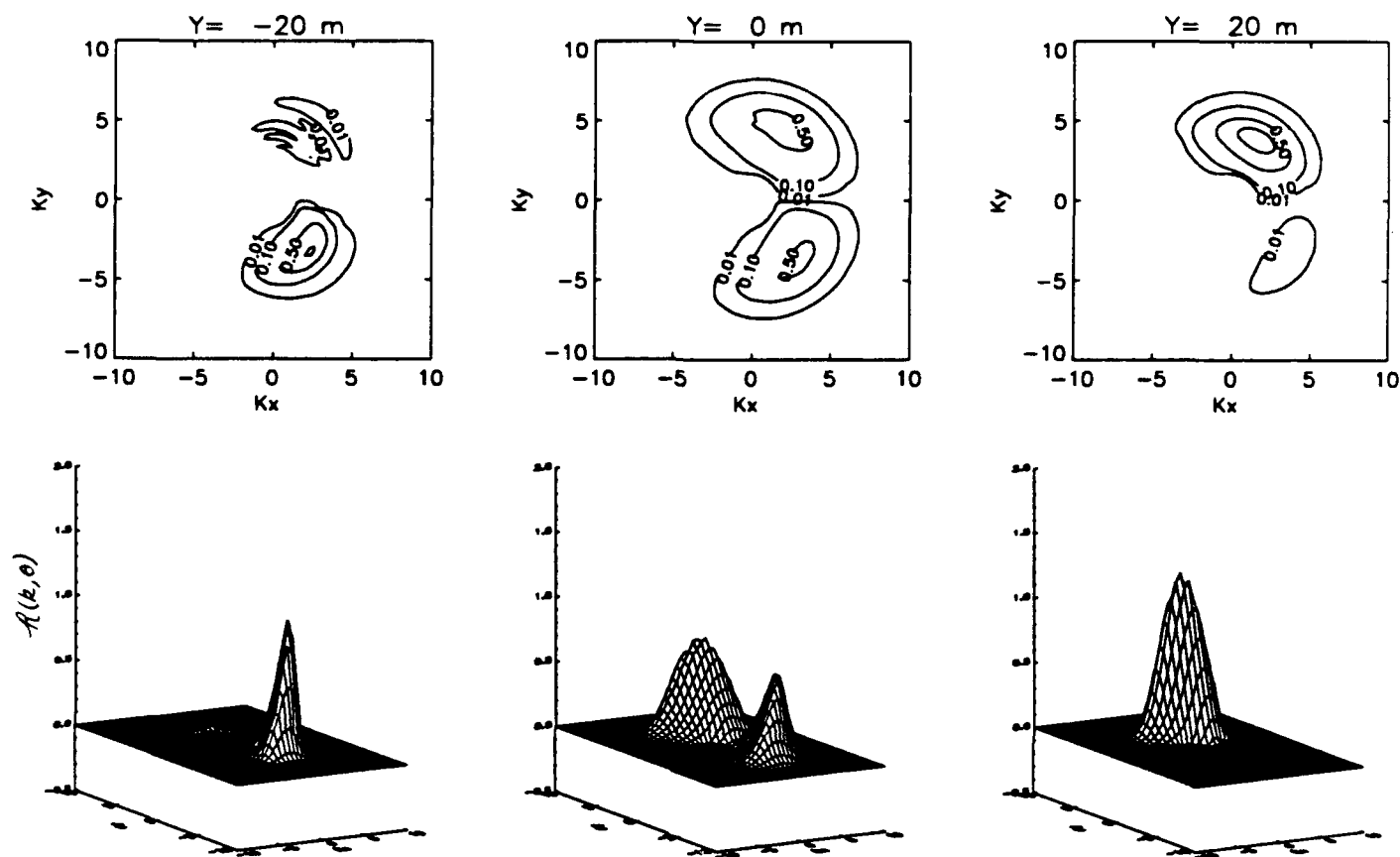


Fig. 11a. NTOW model contour and surface plots of equilibrium fractional difference spectrum $R(k, \theta)$ for 3 m/s winds blowing toward $\theta_w = -20^\circ$ across the Rip. R is shown at $y = -20$ m (south side), $y = 0$ m (center), and $y = 20$ m (north side). The axes are the dimensionless numbers $Kx = \ln(k/k_{\max})\cos\theta$, and $Ky = \ln(k/k_{\max})\sin\theta$, where $k_{\max} = (2\pi/.001) \text{ m}^{-1}$. The Rip parameters are $a = .5 \text{ m/s}$, $b = .1 \text{ m/s}$, $c = .4 \text{ m/s}$, $\delta = 10 \text{ m}$.

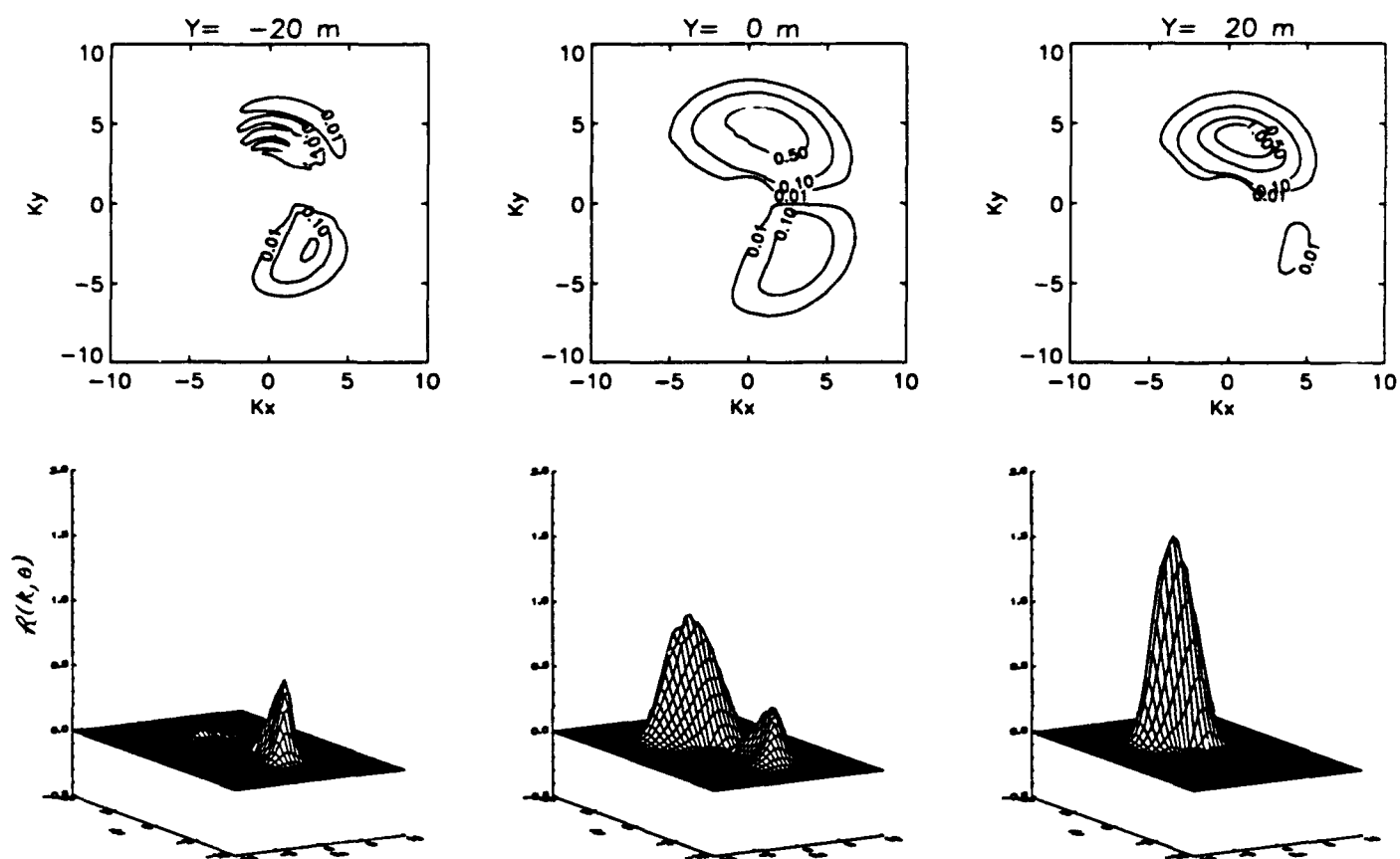


Fig. 11b. As in Fig. 11a, but for $\theta_w = 45^\circ$.

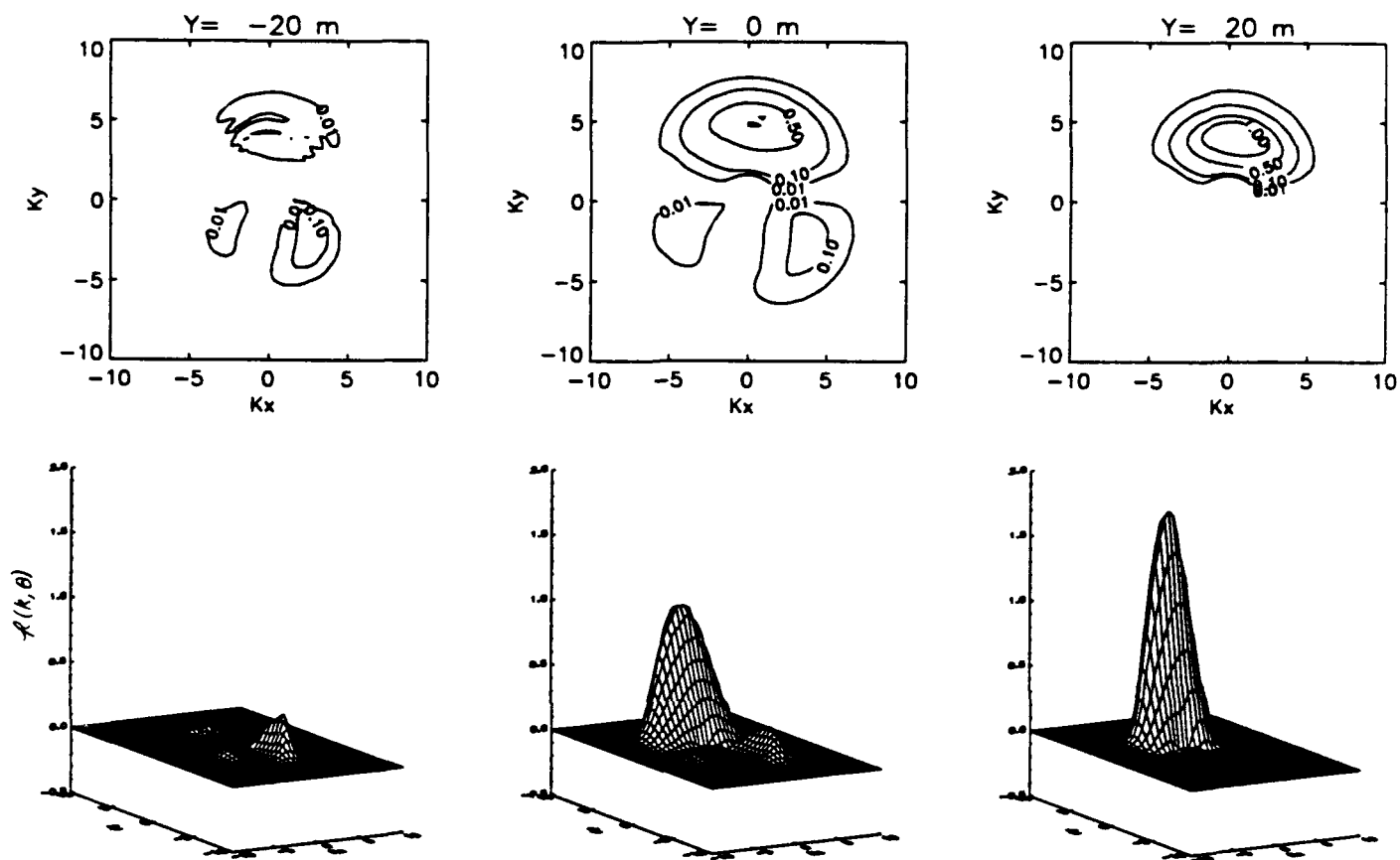


Fig. 11c. As in Fig. 11a, but for $\theta_w = 70^\circ$.

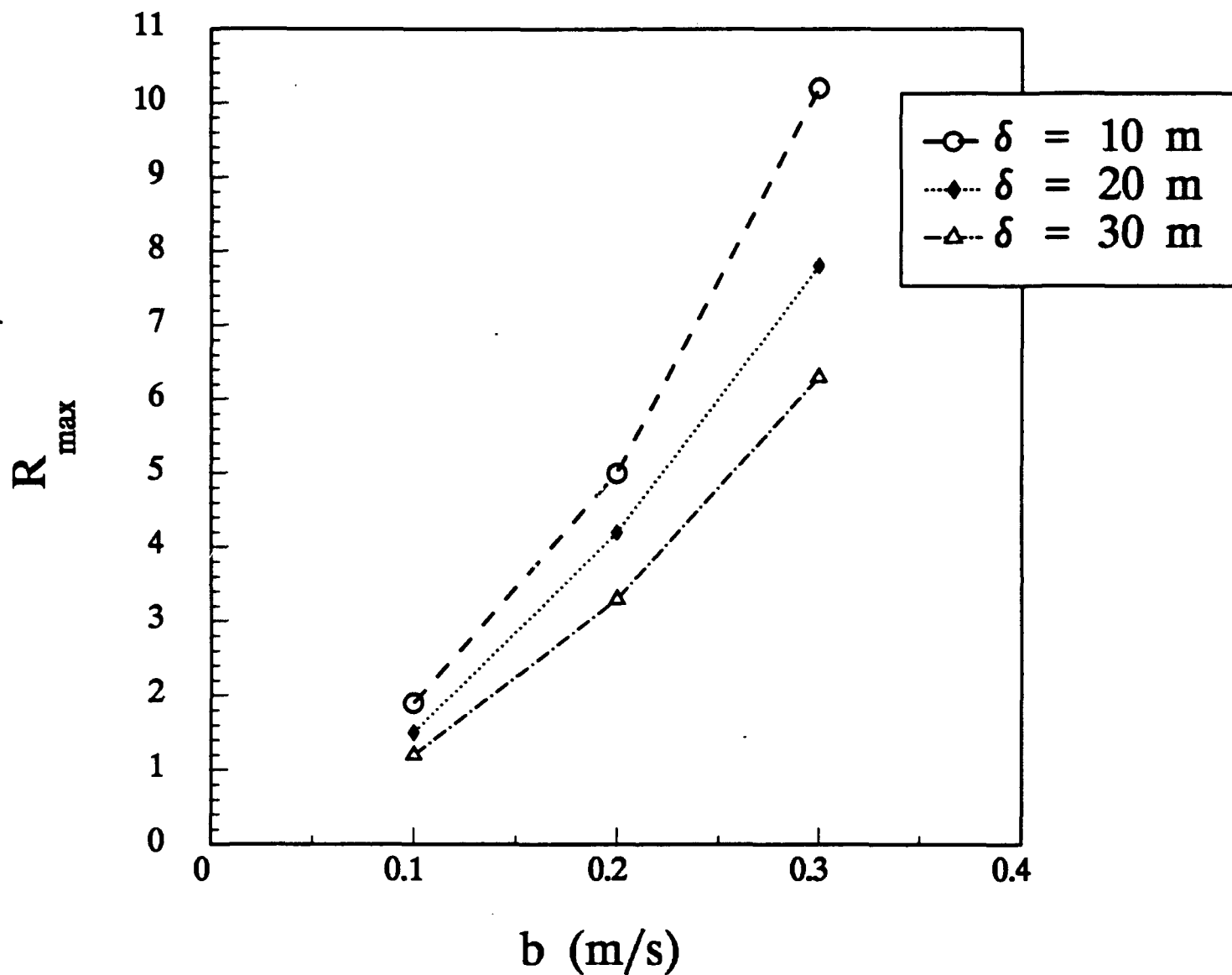


Fig. 12. NTOW model plot of maximum fractional difference spectrum $R_{\max}(k, \theta)$ for several different combinations of the Rip parameters b (convergence speed) and δ (convergence zone width). The wind is 3 m/s blowing toward $\theta_w = 45^\circ$ across the Rip.

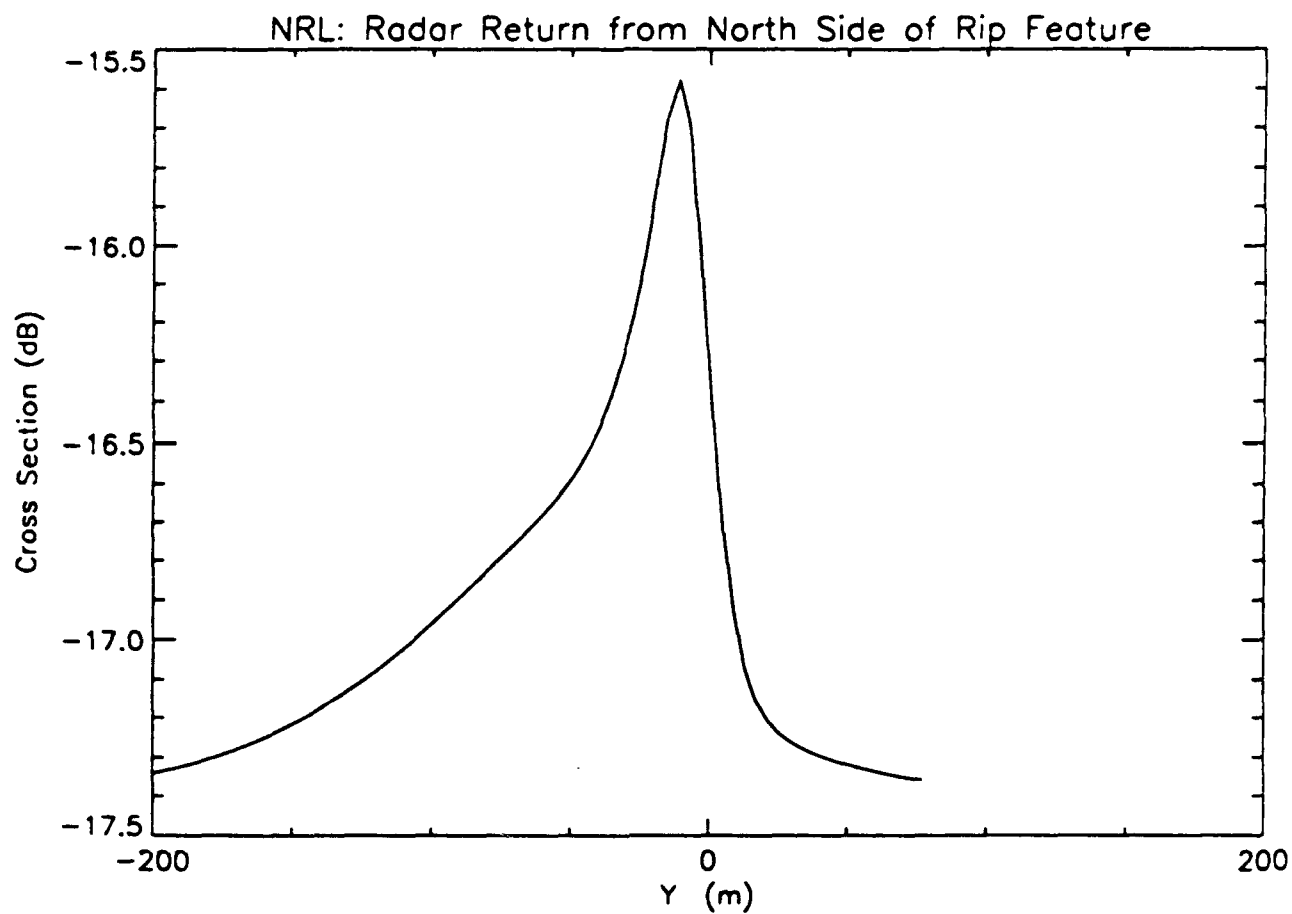


Fig. 13. X-Band HH-RAR cross section per unit area at 37° incidence for standard Rip parameters: $a = .5$ m/s, $b = .1$ m/s, $c = .4$ m/s, $\delta = 10$ m. The flight was parallel to the Rip on the north side. The wind was 3 m/s from 45° south of west.

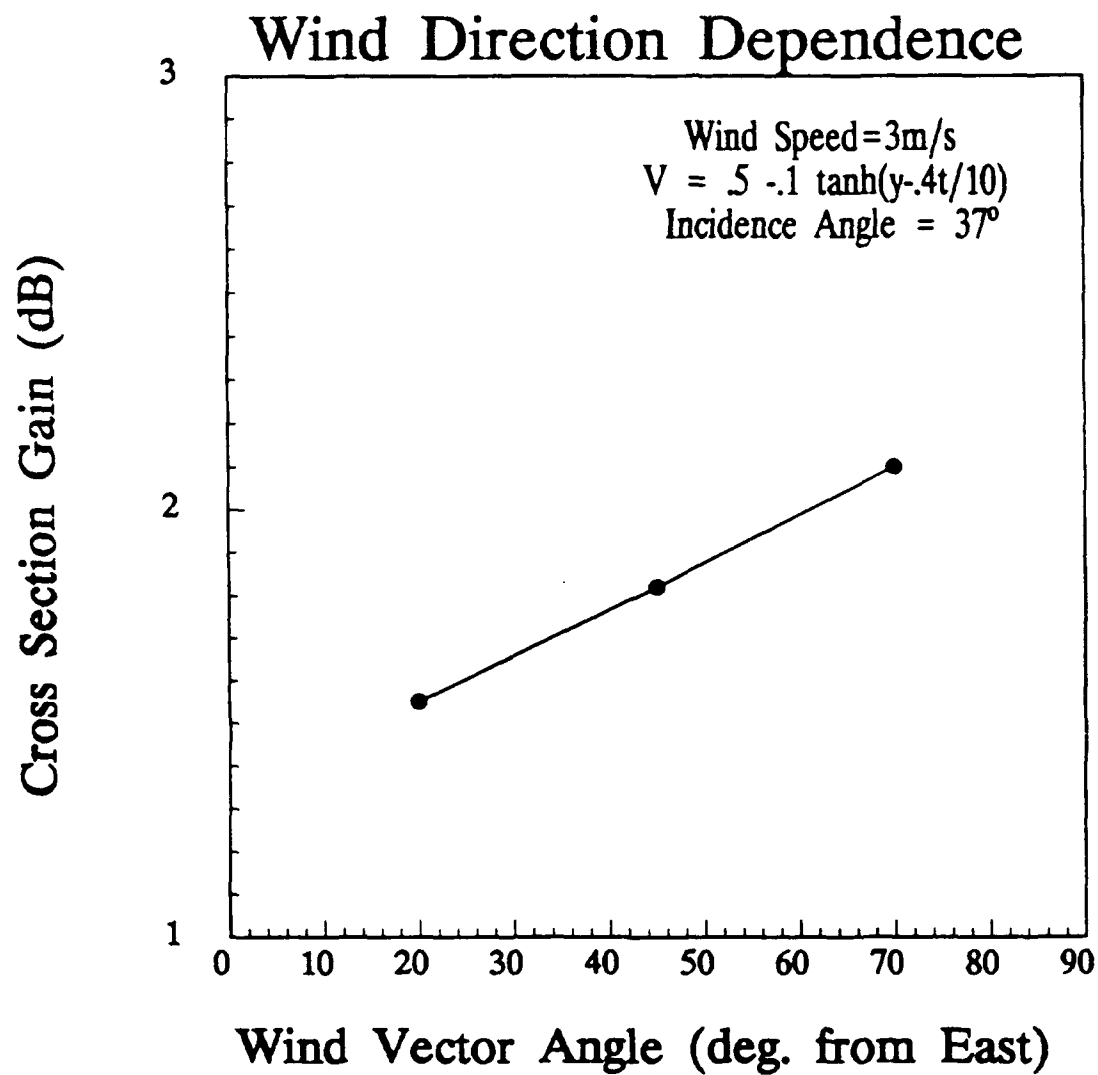


Fig. 14a. Dependence of X-Band HH-RAR return on wind direction for Rip feature.

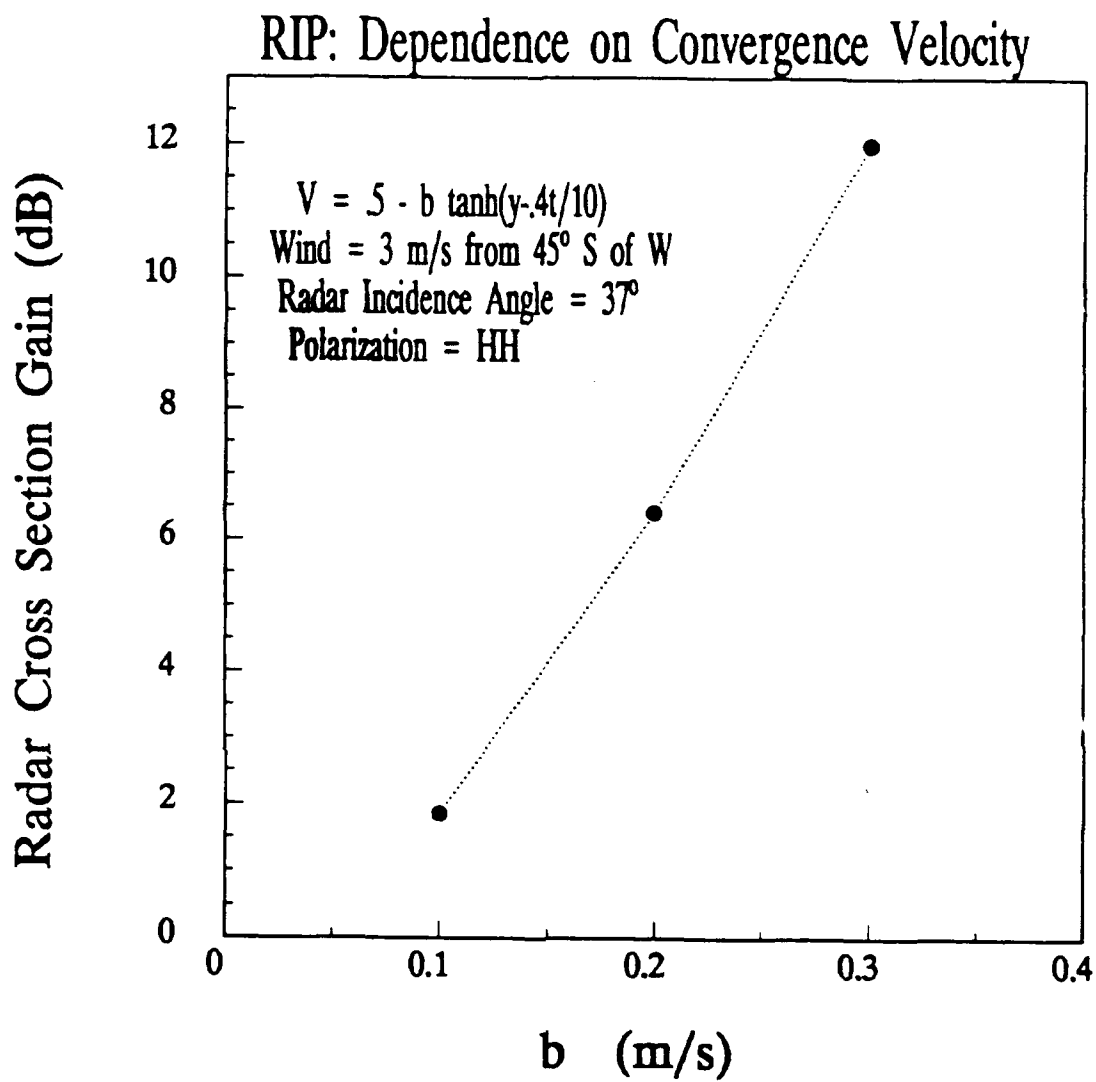


Fig. 14b. Dependence of X-Band HH-RAR return on convergence speed for Rip feature.

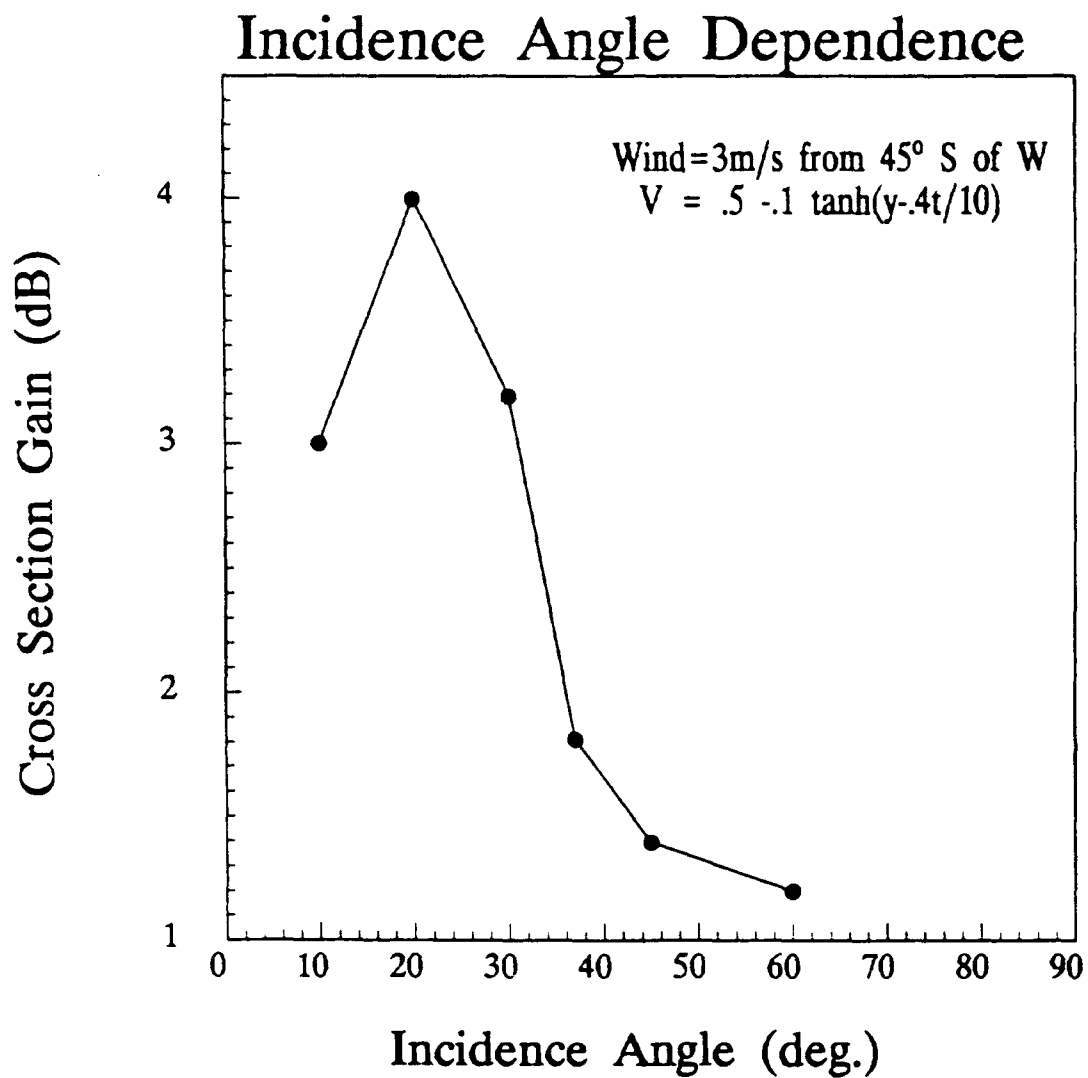


Fig. 14c. Dependence of X-Band HH-RAR return on incidence angle for Rip feature.

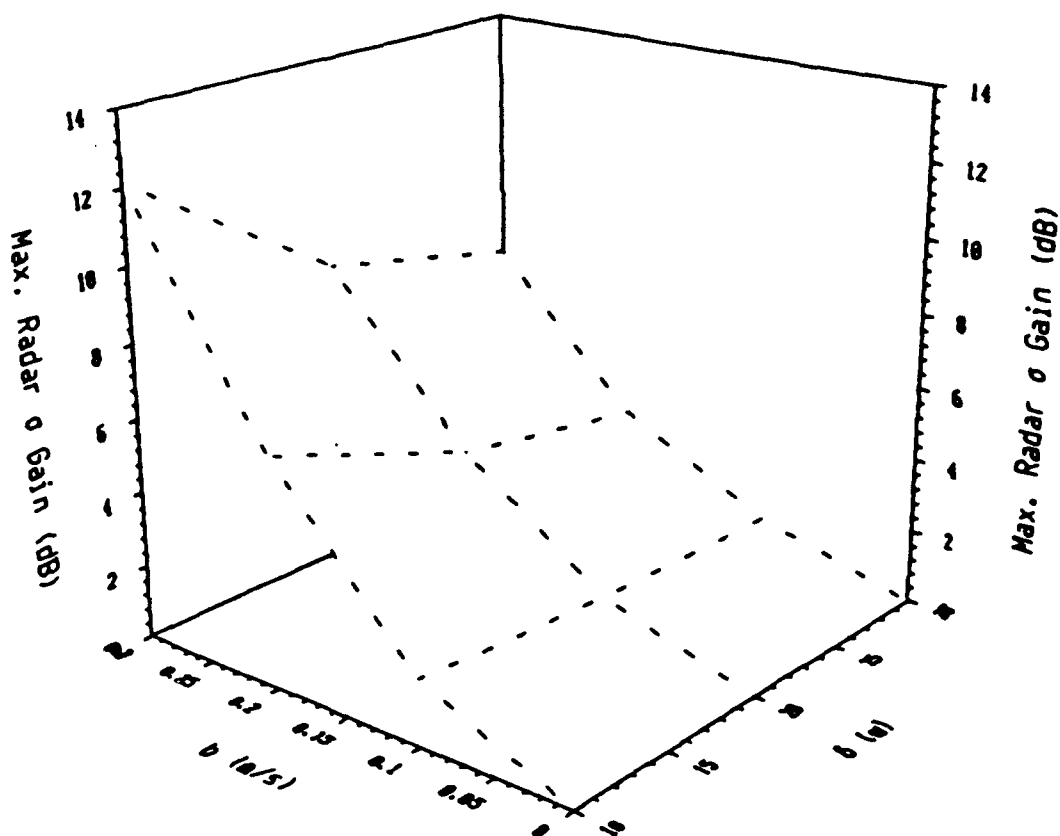


Fig. 15. Surface plot showing the maximum X-Band HH-RAR cross section gain (above background) for variations in the convergence speed (parameter b), and convergence zone width (parameter δ). All other Rip parameters were set to the standard values.

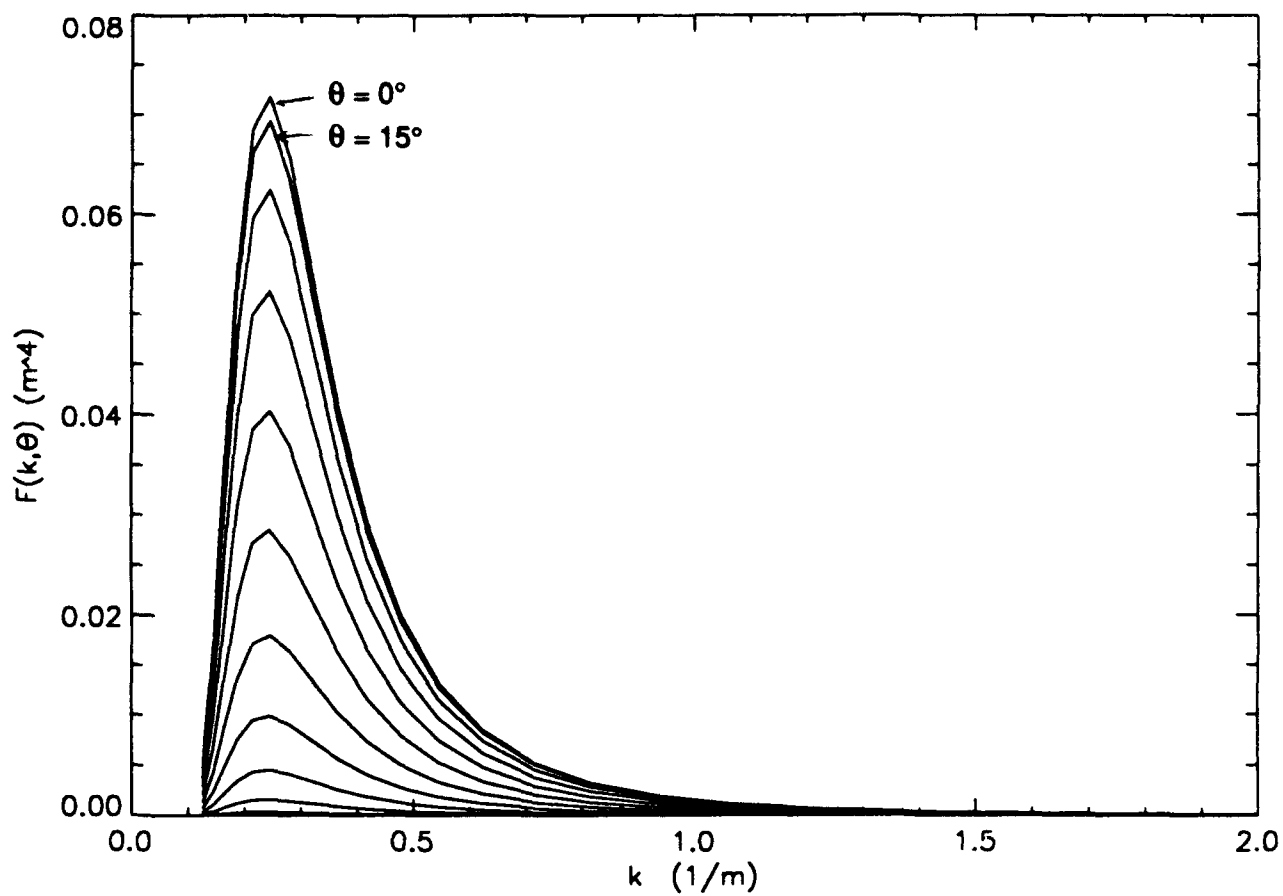


Fig. A1. Equilibrium variance density spectrum $F_o(k, \theta)$ at angles separated by 15° for a wind speed of 5 m/s.

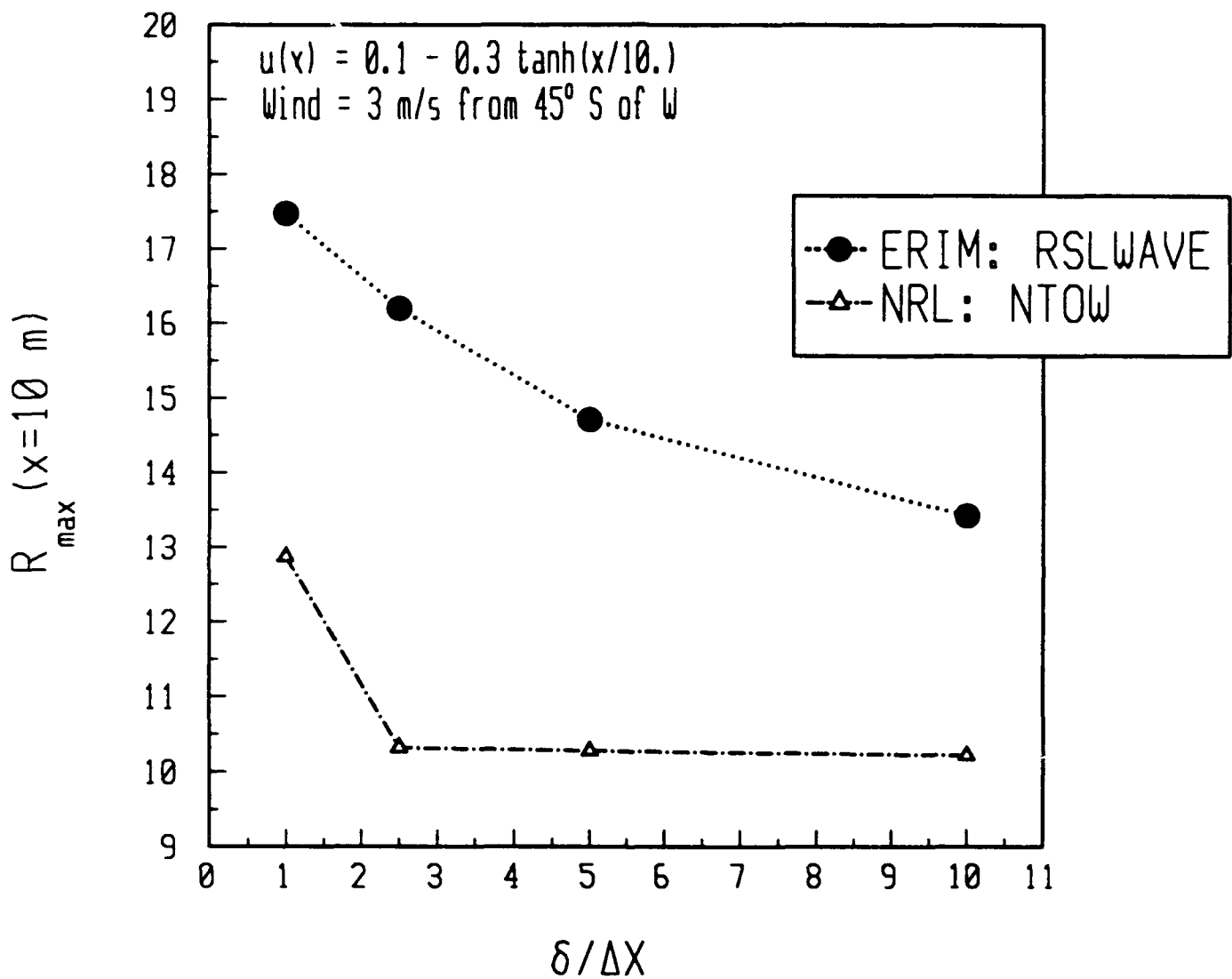


Fig. B1. Peak value in the fractional difference spectrum, R_{\max} , at $x = 10$ m, predicted by the models RSLWAVE and NTOW as a function of grid spacing Δx . The Rip current model is used with the parameters $a = 0.1$ m/s, $b = 0.3$ m/s, $c = 0$ m/s, and $\delta = 10$ m. The wind is at 3 m/s from 45° south of west. The peak corresponds to a wavelength of about 1.2 m.